NUMERICAL MODELING FOR VIBRATORY PILE INSTALLATION IN

SATURATED SAND

A Thesis

by

HONG ZHU

Submitted to the Office of Graduate and Professional Studies of
Texas A&M University
in partial fulfillment of the requirements for the degree of

MASTER OF SCIENCE

Chair of Committee,   Charles P. Aubeny
Committee Members,   Jean-Louis Briaud
                        Jerome J. Schubert
Head of Department,   Robin Autenrieth

May 2020

Major Subject: Civil Engineering

ABSTRACT

In offshore engineering, especially for the construction of offshore wind farms, vibratory driven piles are increasingly appealing. Compared with conventional impact piles, vibratory piles have the advantages of less noise pollution and faster penetration rate. In some specific cases, to meet the requirements of the projects, such as the noise level, the penetration time, and the disturbance to the environment, it is necessary to use the vibratory piles. However, the current level of understanding of the mechanics of vibratory pile installation is incomplete and more reliable predictive models are needed. Thus, a substantial need exists for a better understanding and improved prediction models for vibratory pile installation.

This thesis first summarizes the historical development in vibratory pile driving and then develops a Wave Analysis & Stiffness Degradation Model (WASD) to study the nonlinear behavior of saturated sands during vibratory driving. This model features a hyperbolic constitutive model to characterize non-linear stress-strain behavior together with a cyclically-induced excess pore pressure model by Dobry (1984) to predict wave propagation and degradation in soil strength due to excess pore water pressure during the pile penetration process. The analyses are based on the one-dimensional wave equation theory.

During this study, two cases of using vibratory driving are studied. One is a large steel pile driven in partially saturated sands reported by Dorp (2019), the other case is a sheet pile driven in fully saturated sands by Viking (2002). In the case studies, the

predicted penetration times from the WASD model are compared with the actual results. Then the sensitivities of soil strength reduction to different pile-related and hammer-related parameters are analyzed by several sets of parametric studies.

ACKNOWLEDGEMENTS

CONTRIBUTORS AND FUNDING SOURCES

Contributors

This work was supervised by a thesis committee consisting of Professor Aubeny and Briaud of the Department of Civil Engineering and Professor Schubert of the Department of Petroleum Engineering.

The mathematical and numerical theories for Chapter 4 was instructed by Professor Aubeny.

All other work conducted for the thesis was completed by the student independently.

Funding Sources

No funding was provided for this study.

TABLE OF CONTENTS

LIST OF FIGURES

x

LIST OF TABLES

CHAPTER I

INTRODUCTION

1.1 Background

In offshore engineering, vibratory piles are an increasingly attractive option for installing foundations for platforms. Vibratory driving is a technique where continuously oscillating eccentric masses that have two effects: they cyclically load the soils thereby reducing the soil resistance to pile penetration, and they generate a dynamic force that, along with the pile and hammer weight, acts to overcome soil resistance and penetrate the pile. Compared with conventional impact piles, vibratory driving has the advantages of faster penetration speed, lower noise pollution, reduction of tool changes, easy extraction, and less fatigue damage to driven piles. The vibratory driving technique has been widely accepted since it was first raised in the 1930s. In the recent ten years, many large projects (such as Hong Kong-Zhuhai-Macau Bridge Project) had gained great success, mainly in eastern Asian and northern Europe, in using vibratory hammers to drive huge monopiles with the length up to 70m (230ft) and weight up to 280tons (Rob et al., 2019).

However, compared with what is known about impact driving, the understanding of vibratory driving techniques is still in its infancy. This is mainly due to the limited amount of systematic studies performed, the lack of research generally, and the complexity of the technique (Viking, 2002). The practical application in industries, such as the selection of piles and hammers, mostly depends on experience. Although some studies (Holleyman 1997, Rausche, 2017 and Viking, 2002) analyzed the nonlinear soil behavior under cyclic loading and simulated the process, few of them succeeded in giving a

1

comprehensive and quantitative illustration in the penetration process as well as the soil fatigue.

Hence, to develop a deeper understanding of the soil behavior under vibratory pile driving, the numerical analysis study on the installation of vibratory piles is of significance.

1.2 Problem statement

In the dynamic condition, the pile and the surrounding soil could be regarded as elastic materials. During the process, pore pressure raises, the effective stress decreases, and thus, the soil resistance at the shaft and tip reduces. Soil strength degradation is a continuous process. And when the total resistance from the shaft and tip is equal to the sum of the vertical centrifugal force generated by the eccentric masses and the total weight of all the vibratory parts, the pile penetrates. As shown in Fig.1, under the action of continuous vibration, the energy is transmitted from the pile to the surrounding soil in the form of waves. The waves propagate away in both radial direction and axial direction, causing the continuous movement of the soil particles. The continuous movement rises the pore water pressure between soil particles and reduces the stiffness of the surrounding soil. A complete analysis of the two-dimensional problem requires consideration of soil resistance from both the pile shaft and the tip.

To simplify the complicated process, this study decouples the problem into two one-dimensional problems. The first focuses on radial wave propagation and the concomitant cyclically-induces pore pressure accumulation and the soil resistance reduction. Based on the reduction in soil strength along the pile shaft, the second component of the model simulates the process of penetration as the weight of the pile and

hammer along with the dynamic force applied by the hammer work to overcome soil resistance. Additionally, a rigid pile is assumed.
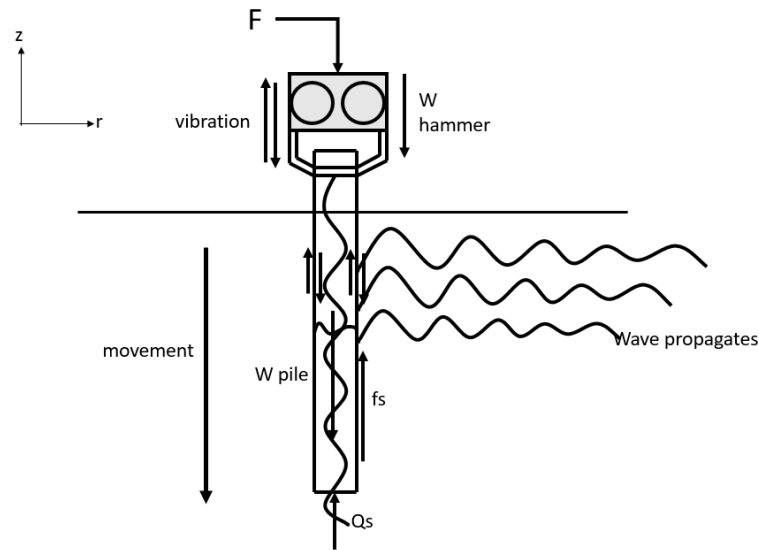
Figure 1 Process of vibratory driving

1.3 Objective of the study

Due to the lack of a comprehensive theory on vibratory piles and the uncertainties in predicting the driving process, it is of significance to gain a more comprehensive understanding of vibratory piles. As a result, the first step of the research is to collect and sort out the previous achievements on vibratory pile installation. Then, based on some experimental results by previous researchers, this study develops a finite-difference model combining with the earthquake engineering knowledge to analyze the pore pressure generation and soil strength degradation. The penetration time with different soil profiles

and hammer types should also be computed and compared, to provide quantitative guidance on the selection of pile and hammer types for a specific soil profile.

In conclusion, the objectives of the study are listed:

1. Understanding the practical and analytical fundamentals of vibratory pile driving, collecting and organizing the previous work on vibratory piles

2. Programming a 1-D wave analysis and stiffness degradation model for vibratory driving

   a. Simulating the accumulation of excess pore pressure during the cyclic loading from the pile vibration.

   b. Studying degradation of the stiffness of surrounding stiffness.

   c. Computing the penetration time.

   d. Carrying out case studies to verify the effectiveness of the model.

   e. Investigating the sensitivities of penetration time to different sizes of hammers and piles.

1.4 Organization of the study

This study includes five chapters. The second chapter commences with a historical review of the application of vibratory driving techniques and then illustrates the principles behind the implementation of vibratory equipment and the key parameters generally used to characterize the drivability.

Chapter 3 gives a review of the analytical background of the research. Some fundamental theories in earthquake engineering, such as the wave propagation theory, are introduced. This chapter presents some nonlinear constitutive soil models which are

4

suitable for simulating the soil stress-strain behavior under cyclic loading. And then, it describes some pore pressure models concluded from previous experimental tests. The pore pressure models provide a source for the calculation of excess pore pressure caused by vibration.

Chapter 4 introduces the principles of the one-dimensional wave propagation model, including the numerical methods, the boundary conditions, the constitutive model, and the pore pressure model.

Chapter 5 are two case studies based on the CPT results published by Dorp (2019) and Viking (2002). The graphs in this chapter show the comparisons between the predicted penetration times and the actual penetration times.

Chapter 6 includes several sets of parametric studies. This chapter represents the pore pressure accumulation and the soil friction degradation during vibratory driving, as well as the penetration time for different hammer sizes, pile sizes, and soil types. Based on those results, the sensitivity of the drivability to various parameters is manifest.

Chapter 7 concludes the study, reissues some assumptions made in this study to simplify the problem and outlines some further work to modify the model.

CHAPTER II

FUNDAMENTALS OF VIBRATORY DRIVING TECHNIQUES

2.1 Introduction

During vibratory pile driving, the penetration of pile is mainly produced by the reduction of internal friction angle and the generation of pore-pressure after the high-frequency vibration. Compared with the traditional impact piles, vibratory driven piles have some different characteristics in practical driving, and the differences are listed in table 1. Because of those traits, vibratory driven piles have the following advantages: less energy loss because of the rigid pile-hammer connection, faster penetration speed, lower noise level, and the reduction of the pile fatigue damage during installation. (Dorp, 2019) However, vibratory driving also has limitations such as the low bear capacity at the end of the installation and the undesirable vibrations to the nearby structures (Rausche. 2002) Therefore, for a specific case, whether to choose a traditional pile or a vibration pile needs to be determined according to the primary task of the project. For example, for projects in weaker soil layers with tight construction schedules or projects that need to reduce the impacts on surrounding wildlife or urban residents, vibratory piling should be selected. While for those projects in hard soils, with sufficient time or without vibratory driving conditions, the traditional impact driving or other methods should be used.

Table 1 Practical differences between impact piles and vibratory piles

Impact driving	Vibratory driving
Low frequency and high peak force	High frequency and low peak force
No tension between hammer and pile	Rigid connection between hammer and pile
Intermittent energy to pile and soil	Continuous energy to pile and soil
Penetration by high load force	Penetration by reduction of internal friction or accumulation of pore water pressure

This chapter gives a review of the development history of vibratory driving techniques. It presents an introduction to the basic theory as well as the operation principle of vibratory driving. Summaries of each following section are given below:

Section 2.2 reviews the history of the application of vibratory techniques as well as the findings of the studies on soil behaviors under vibratory driving.

Section 2.3 introduces the essential components of the vibratory hammer and the function of each element.

Section 2.4 outlines some main vibrator parameters that are crucial to the pile-drivability and deduces operation formulas from Newton's second law.

Section 2.5 illustrates the principle of penetration during pile driving in different soil types.

2.2 Developments of vibratory driven piles

2.2.1 Developments of vibratory driving techniques

The history of vibratory driving techniques started from the 1930s in Germany and Russia. (Viking, 2002) Its applicability was recognized rapidly, and the technology was spread into France, Japan, and the United States in the 1950s after its first commercial application in Germany in 1932. In 1957 Barkan reported the dramatic reduction of shaft friction during vibratory driving. And later, he pointed out the resonance effect to increase the driving ability. At almost the same time, Bodine initially applied a high-frequency (more than 100Hz) vibrator hammer called Bodine Resonant Driver based on the effect of resonance. The increasing frequency significantly improved the rate of penetration.

With the development of applied technology, theoretical research began to flourish. During the 1960s, several different research projects (Hill (1966), Ghahramani (1967), Yang (1967), and Griggs (1967)) were initiated to study the penetration resistance and bearing capacity of vibratory-driven piles. In 1960, Smith represented the soil-pile interaction by a series of springs and dashpots, and he was the first to regard the pile as elasticity to analyze the process of pile installation (Fig. 2) by the wave equation. Based on his work, many researchers (Lowery 1967, Chua 1987, Raushche 2002) modified the approach, simulated the hammer-pile system, and clarified the influential factors to the drivability of vibratory pile in their studies. In 1972, a program WEAP was developed to simulate the dynamic behavior of impact hammers and piles. Compared with the pile-driving formulas widely used before, the pile is no longer regarded as rigid.

However, the associated soil behavior problems are not completely solved. Some numerical driving studies (Holeyman et al. 1996, Holeyman 1985 and 1997, Allani and

Holeyman 2013, Denies and Holeyman 2016, Leonards 1995, Chrisopoulos 2019) were conducted at the end of 20th century by using integration methods, finite element methods, and discrete element methods to analyze the resistance in soil-pile interaction surface of saturated and dry granular soils. Holeyman conducted in-depth modeling research on the influence of pile driving parameters on the pile driving efficiency through experiments. His research results show that the analysis of high-frequency vibration pile driving considers the influence of pile, vibration pile hammer, and foundation soil. The pile-soil interaction mechanism under high-frequency vibration load is more complex, which is different from the response characteristics of conventional pile driving.
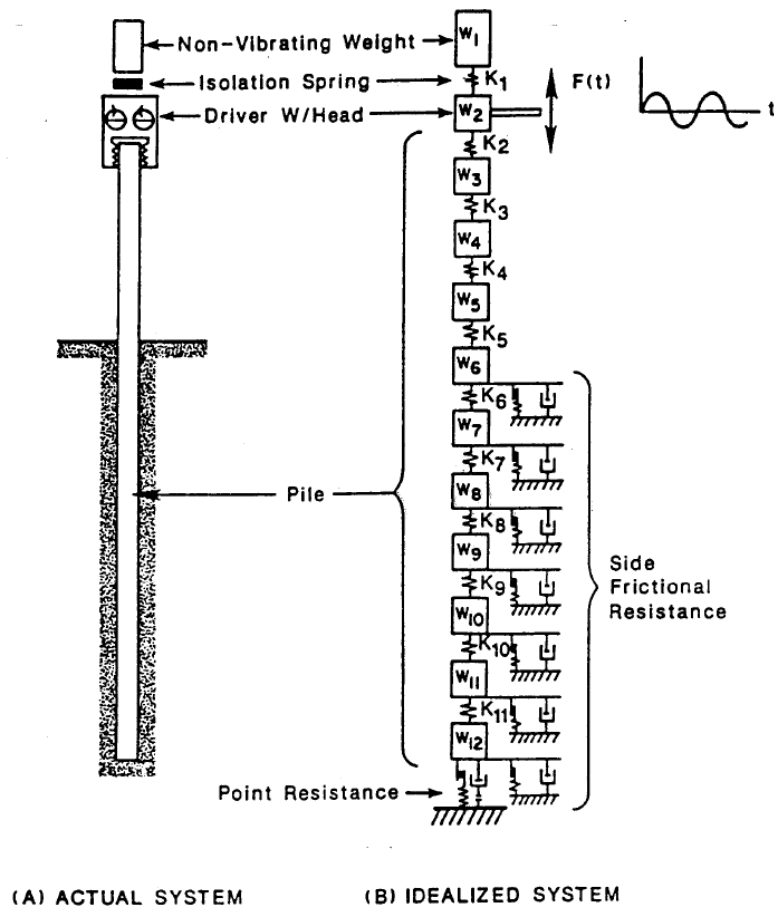
Figure 2 Wave equation model in a pile vibratory driving (Garner, 1987).

9

2.2.2 Developments of soil liquefaction theory

The potential liquefaction of soils is the main reason for the reduction of soil strength during the vibratory pile driving. To understand the soil's weakening process during vibration, we need to comprehend the soil liquefaction theory first. From the late 1970s, the research on liquefaction during vibration has gained much attention. The qualitative understanding of the liquefaction has been considerably enhanced. Several researchers have conducted stress-controlled or strain-controlled experimental tests to investigate the dynamic soil responses to the regular harmonic excitations (Ishibashi (1977), Dobry (1982), and Finn (1981)).

In 1975, Martin, et al. presented a method relating the volume change of dry sands under cyclic loading to the pore-pressure build-up in the same sand for the saturated undrained condition. Based on a large number of triaxial cyclic test results, Seed, Martin, and Lysmer (1976) developed a pore pressure model representing the relationship between the increase of pore pressure and the number of cyclic loadings, which is a mile mark in the research of liquefaction potential.

2.3 Basic components of the vibratory hammer

As is shown in Figures 3 and 4, the vibratory pile-hammer systems (either the free-hanging system or leader mounted system) are composed of two main parts: the power source part and the exciter part. The power source part is motivated to generate diesel force or hydraulic force and provides energy for the exciter. The exciter has several components:

one or several pairs of eccentric masses oscillated to create the vibration forces, an oscillator powered by the hydraulic or diesel motor, a suppressor (hammerhead) providing the static surcharge force; and a hydraulic clamp to rigidly connect the pile and hammer.
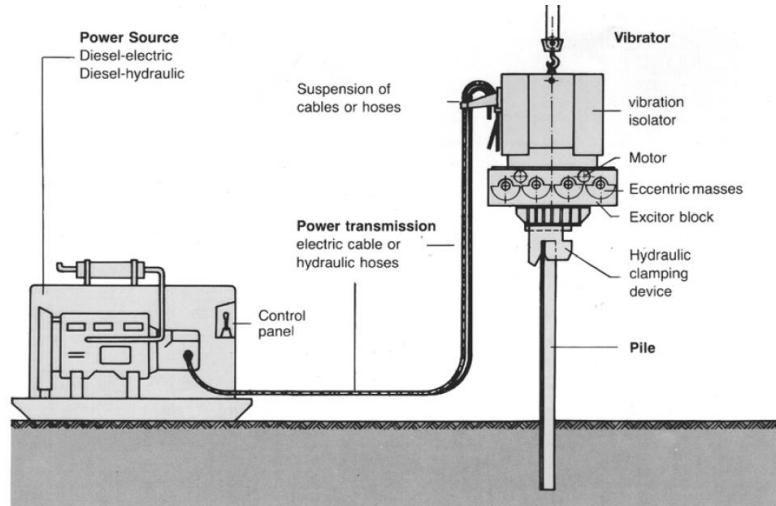
Figure 3 Components of a free-hanging vibratory-machine system (Viking, 2002)
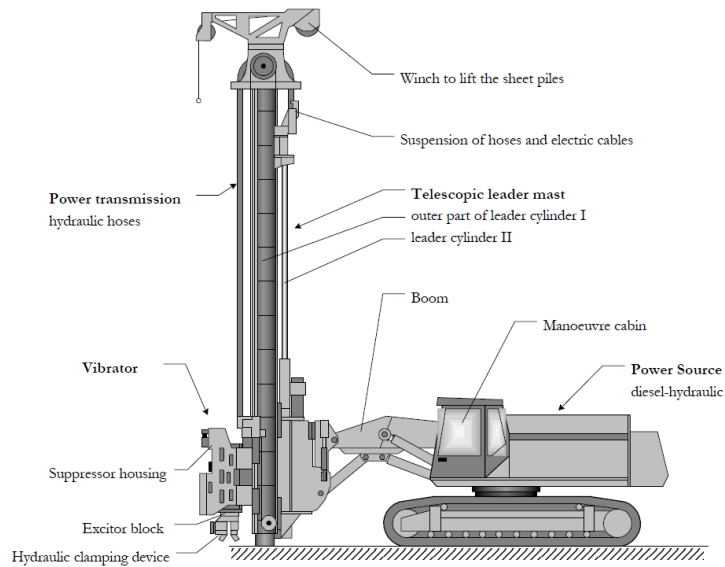
Figure 4 Components of a leader-mounted vibratory-machine system (Viking, 2002)

There are two types of vibrators: hydraulic and electrical. Typically, the hydraulic vibrators are smaller and lighter than the electrical counterparts. The selection of different vibrators should consider the following aspects:

a. Drivability aspect: select the proper vibrator to obtain the optimal rate of penetration.

b. Environment aspect: minimize the damage and noise caused by vibration and the disturbance to the wildlife.

c. Bearing capacity aspect: make sure the expected bearing capacity at the end of the installation can be reached.

Based on experience and fieldwork, Rodger and Littlejohn (1980) have given a recommendation on the vibrator parameters for various application cases, as shown in Table 2.

Table 2 Vibrators Classification (Rodger and Littlejohn, 1980)

Cohesive soils	Dense cohesionless soils		Loose cohesionless soils	
All cases	Low point resistance	High point resistance	Heavy piles	Light piles
High acceleration Low displacement amplitude Predominant side resistance Requires high acceleration for either shearing or thixotropic transformation	High acceleration Predominant side resistance Requires high acceleration for fluidization	Low frequency. Large displacement amplitude Predominant side resistance Requires high displacement amplitude and low frequency for maximum impact to permit elastoplastic penetration		High acceleration Predominant side resistance Requires high acceleration for fluidization
Recommended parameters				
v > 40 Hz a: 6-20 g s: 1-10 mm	v: 10- 40 Hz a: 5-15 g s: 1-10 mm	v: 4-16 Hz a: 3-14 g s: 9-20 mm		v: 10- 40 Hz a: 5-15 g s: 1-10 mm

When it is operating, the eccentric masses rotate to generate harmonic vertical forces typically at frequencies between 20 to 30 Hz (Chua, 1987; Jonker, 1987). The clamps transmit the hammer movement to the pile, and the high-frequency forces motivate the movement of the pile. During the oscillating of the eccentric masses, the horizontal forces are canceled, and the vertical forces are added. (Fig. 5)
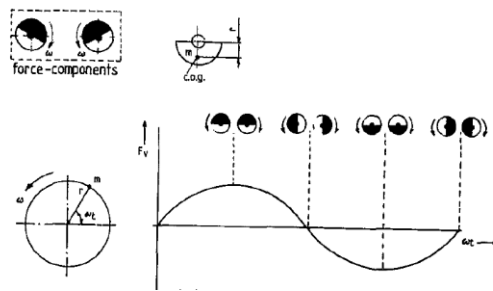
Figure 5 Operation of eccentrics (Jonker, 1987)

2.4 Influence factors of vibratory pile drivability

The penetration capability and rate of the vibratory pile are influenced by factors from the three aspects: the pile-related parameters, the vibrator-related parameters, and the soil-related parameters. The pile-related parameters include the pile weight and pile size. The increase of pile weight raises the driving force, while the increase of the pile size leads to higher resisting forces. The vibrator parameters such as the frequency, the eccentric moment as well as the weight of the hammer are critical. The frequency largely influences the dynamic driving force. However, there is no conclusion on how to select the optimal vibration frequency based on the specified pile and soil profile. Massarsch (2017) reported that at the resonant frequency, the vibration rate of the pile is maximum, but the relative

movement between the soil and pile is minimum, so the rate of penetration is slow as well. When it goes beyond resonance, the penetration rate increases with the frequency. So, we should avoid the resonance frequency when selecting the hammer parameters. The resonance frequency is a function of the shear wave speed, and in most cases, ranging from 20 to 30Hz. Figure 6 shows the relationship between the relative displacement and frequency. Us is the displacement of soil, and Up is the displacement of the pile.
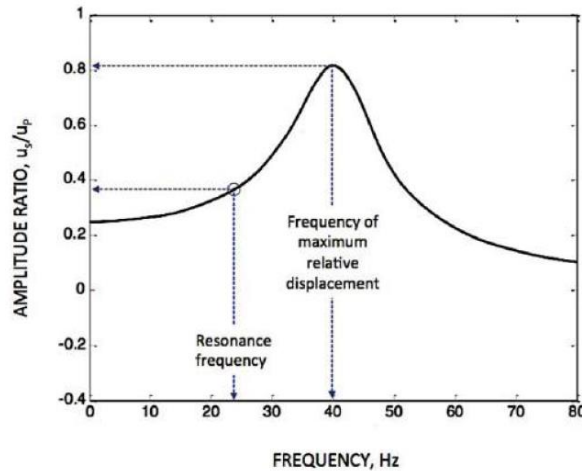
Figure 6 Amplitude ratio of soil/pile displacement vs. frequency

The eccentric moment is related to the vibration amplitude, which governs the magnitude of excess pore pressure. As for the soil-related parameters, the strength, density, relative density, and void ratio of soils are important to the driving capability and the penetration speed. The following equations can be deduced from Newton's Second law: The eccentric moment is given by:

$$M_{ecc} = \sum m_e * r \qquad (2.1)$$

14

where M_{ecc} = eccentric moment (kg*m)

m_e = mass of the eccentric mass (kg)

r = eccentric radius [m].

The maximum centrifugal force:

$$Fc = \sum m_e * r * \omega^2 \tag{2.2}$$

where Fc = maximum centrifugal force (N),

ω = angular frequency (rad/s)

The vertical component of the centrifugal force:

$$Fv = Fc * sin\theta = \sum m_e * r * \omega^2 * sin\theta \tag{2.3}$$

The angular frequency can be calculated from the frequency:

$$\omega = 2\pi f \tag{2.4}$$

where f = vibration frequency (Hz),

The total weight of dynamic parts (sum of all the oscillating components):

$$w_{dynamic} = w_c + w_p \tag{2.5}$$

where w_c = weight of the exciter case and the clamps (N)

w_p = weight of the driven pile (N).

$w_{dynamic}$ = total weight of the dynamic parts (N)

The single amplitude of vibration:

$$A = \frac{M_{ecc}}{m_{dynamic}} \tag{2.6}$$

According to O'Neill and Vipulanandan (1989a), the empirical equation, though

not proven, suggests the driving frequency should be picked by:

$$f \leq \frac{\sqrt{\left(\frac{E}{\rho}\right)}}{20L} \qquad (2.7)$$

where f = driving frequency (Hz)

L = length of the pile (m)

E = Young's modulus (N/m2)

ρ = density of the pile material (kg/m3)

2.5 Principles of soil failure during pile penetration

A few hypotheses are brought up to explain the soil failure principles both along the shaft and at the tip during the pile penetration. During the cyclic vibration, the soil resistance degrades, and the pile penetrates when the total resistance at the tip and shaft is less than the sum of the total weight of the vibrator-pile system and the downward vibration force.

According to Massarsch (2017) and Jonker (1987), the mechanism of the soil failure in cohesionless soils and cohesive soils are different. In my opinion, the reduction of soil strength is mainly resulting from two reasons: the reduction of friction angle or/and the generation of excess pore water pressure.

In the process of vibratory pile driving, the soil skeleton is affected by the inertial force under the action of the exciting force. When the stress intensity exceeds the strength of the skeleton, the original connection strength and structural state of the soil particles are destroyed. The soil particles are rearranged, resulting in volumetric deformation, as well as the stresses redistributed. At this time, the pressure transmitted by the soil particles through the contact point is taken by the pore water, which causes the pore water pressure

16

to increase. Under the combined action of self-weight and excess water pressure, the pore water pressure gradually accumulates with the increase of loading cycle times. On the one hand, the pore water is discharged upward under the action of excess hydrostatic pressure; on the other hand, the soil particles try to move downward under the effect of gravity. When the two are equal, the soil particles are in suspension, and then the effective stress on soil skeleton is zero, the saturated sands behave like liquids and cannot bear any shear, so soil liquefaction occurs.

CHAPTER III

ANALYTICAL BACKGROUND: BASIC SOIL DYNAMICS

3.1 Introduction

In this chapter, the analytical background theories in soil dynamics and earthquake engineering, on which our vibratory pile driving model is based, are introduced.

Section 3.2 demonstrates the one-dimensional wave propagation theory and reveals the relationships between various wave parameters. Then the wave equation theory is illustrated, and some wave equation analysis studies are reviewed.

Section 3.3 explicates the excess pore water pressure accumulation during cyclic loading and the potential to liquefaction. Then lists and introduces several pore pressure models.

 Section 3.4 gives a review of the soil stress-strain behavior and emphasizes on the nonlinear response of soils under cyclic loading.

3.2 One Dimensional Wave Propagation

The energy produced by the hydraulic or electric motor is transferred to vibrate the hammer-pile system. The energy travels along the pile and spreads away into the surrounding soil from the shaft and the tip, causing the continuous movement of the soil. In this process, the soil absorbs energy to overcome the self-weight and resistance between particles, which is called damping. The energy propagates in the form of waves, decays with time and distance because of the damping, and eventually dissipates in far-field.

3.2.1 Categories of Waves

We call the motion formed by the disturbance or vibration of a certain physical quantity transmitted point by point in space as waves. The waves induced by the pile installation can be regarded as a kind of seismic waves produced by an artificial source.

According to the modes of propagation, the waves are divided into surface waves and body waves. Surface waves travel along the ground surface and diminish as they get further from the surface. Body waves travel through the interior of soils, and there are two types of body waves: primary waves (P-waves) and secondary waves (S-waves). P-waves are longitudinal waves traveling along with volume changes of soils. The motion of soil particles is in the same direction as the wave propagation. S-waves are transverse waves associated with the distortion of soils instead of volume changes, the motion of the soil particles is perpendicular to the direction of wave propagation. The diagrams of S-waves and P-waves are shown in Fig.7. During the vibratory pile driving, P-waves travel axially through the pile and cause the compression of the pile, and S-waves travel radially into the soil.
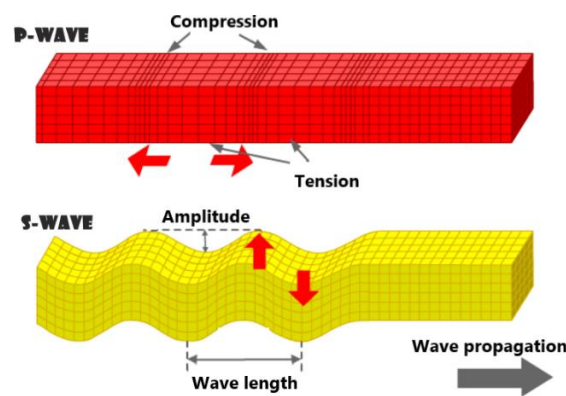
Figure 7 P-waves and S-waves

3.2.2 One Dimensional Sine Wave

Without considering the energy loss and dispersion, the shear wave propagation in soils is considered as a definite simple harmonic motion (Fig.8). The sine wave is described as:

$$u(x, t) = A \sin(kx - wt + \emptyset) \tag{3.1}$$

where A is the amplitude of the wave, k is the wavenumber, w is the angular frequency, and $\emptyset$ is the phase constant. The wavelength λ is the distance between two sequential crests or troughs.
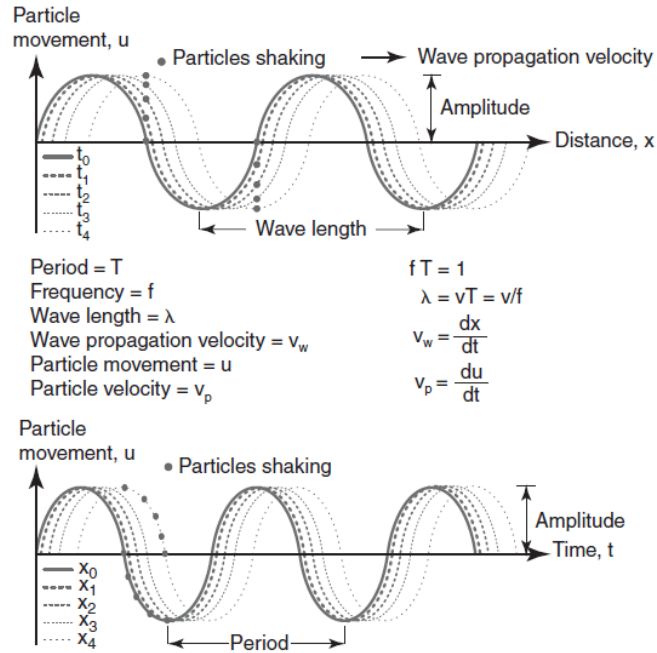
Figure 8 Single wave propagation (Briaud, 2013)

The wavenumber and wavelength have the relationship:

$$k = \frac{2\pi}{\lambda} \tag{3.2}$$

The period T is the time for one complete cycle, and f frequency is the number of cycles per second. They are related by:

$$T = \frac{1}{f} \tag{3.3}$$

The angular frequency ω is the frequency in radians per second:

$$\omega = 2\pi f = \frac{2\pi}{T} \tag{3.4}$$

The wave velocity v is the speed of wave propagating in mediums, expressed as the ratio of the wavelength and the period:

$$v = \frac{\lambda}{T} \tag{3.5}$$

In soils, the shear wave velocity can be represented in terms of G (shear modulus) and ρ (density):

$$v_s = \sqrt{\frac{G}{\rho}} \tag{3.6}$$

3.2.3 One-Dimensional Wave Equation

The wave equation is a second-order differential equation to describe the waves in nature. In 1746, d'Alembert discovered the one-dimensional wave equation, and after about ten years, Euler discovered the three-dimensional wave equation. (en.wikipedia.org, 2020) The form of the one-dimensional equation is generally represented as follows:

$$\frac{\partial^2 u}{\partial t^2} = c^2 \frac{\partial^2 u}{\partial x^2} \tag{3.7}$$

21

u(x,t) is the function of the wave that has one space dimension x. c is the wave velocity in the specific medium. For this study, we use v_s to represent the shear wave velocity in soil.

As mentioned in chapter 2, the analysis of the impact pile installation using wave equation has been studied by Smith et al. (1960). He used the discrete elements of the pile to replace the continuous pile and derived five basic formulas from the physical law to replace the differential formula of the one-dimensional wave equation to study the penetration process and the behavior of the impact pile under every blow of the hammer. The pile-soil interaction is represented as a serious of springs and dashpots. However, there are differences in the driving analysis between impact piles (WEAP) and vibratory piles, as shown in table 3. Since the relationship between K, C, and frequency is unknown, the wave equation analysis by WEAP is not suitable for the simulation of vibratory piles.

Table 3 Analytical differences between impact piles (WEAP) and vibratory piles

Impact piles WEAP	**Vibratory piles**
The spring constant K and damping C are independent of frequency	The spring constant K and damping C are functions of frequency
• Penetrates when loading> resistance • Resistance does not change	• Soil weakens due to the reduction of internal friction and build-up of pore water pressure • Penetrates when dynamic weight + dynamic force > resistance after cyclic loading

Besides, Holeyman and Legrand (1997) use a one-dimensional radial discretization model (Fig. 9) to present the radial wave propagation and simulate the nonlinear soil behavior under the vibratory driving force. In his model, the cylindrical surrounding soils are discretized into a set of concentric rings connected by springs transferring forces from one to the neighbor ones. The thickness of the rings increases with radius representing the geometrical damping. As the wave propagates, the rings move vertically, and the springs are compressed.
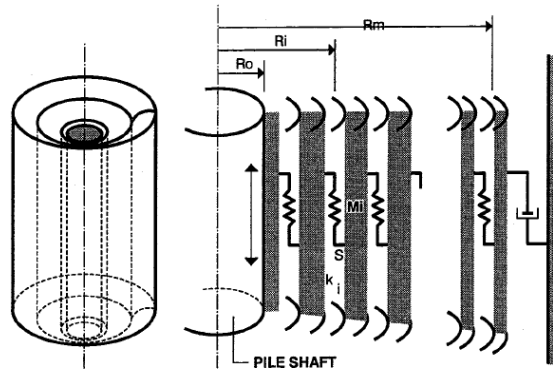
Figure 9 Model Geometry of Holeyman's model (Holeyman, Legrand 1997)

3.3 Pore Water Pressure Generation under Cyclic Loading

Cyclic loading on sands, even in dense sand with a tendency to dilate during unidirectional or monotonic loading, results in a decrease in soil volume. In saturated sands, the pore water pressure is progressively generated and accumulated during the cyclic loading because of the incompressibility of pore water. The increasing speed of pore pressure mainly depends on the relative density (void ratio) of the soil, the stress history(or

23

strain level), and the number of cycles (Dobry, 1982). When the value of excess pore water pressure is equal to the confining pressure, the effective stress becomes zero, and the soil would behave like a liquid, of which the phenomenon is called liquefaction. As mentioned in previous chapters, numerous outstanding works on liquefaction under cyclic loading have been proposed, some empirical pore water pressure formulas and models have been created based on either stress-controlled or strain-controlled undrained cyclic loading tests. Strain-controlled models include those developed by Martin, et al. (1975), Finn (1981), and Dobry (1982), while stress-controlled models include the work of Seed, et al. (1976), and Ishibashi (1977) with further refinements made by Hwang (1995) and Konstadinou (2013). Several pore-pressure models are listed in the following:

3.3.1 Martin et.al. 's model (strain-controlled)

In a pioneering study of pore-pressure generation during cyclic loading, Martin et al. (1975) developed a relationship between the volume reduction of saturated sands in drained cyclic tests and the pore-pressure rise during undrained cyclic tests. They proposed a quantitative formula (eq.3.8) for the potential liquefaction. The behavior of saturated sands under undrained conditions can be predicted from the sand in drained conditions, as will be discussed subsequently.

$$\Delta u = \overline{E_r} \Delta \varepsilon_{vd} \tag{3.8}$$

Δu is the increase in residual pore pressure (the pore water pressure at shear stress = 0) for the cycle; $\overline{E_r}$ is the tangent modulus of the one-dimensional unloading curve at a point corresponding to the initial vertical effective stress; and $\Delta \varepsilon_{vd}$ is the net volumetric strain increment.

24

3.3.2 Finn 's model (strain-controlled)

Finn's formula is developed from Ottawa sand at a relative density D_r=45% during the undrained strain-controlled cyclic simple shear tests for four different strain amplitudes. (Finn, 1981) It is reported that the pore pressure ratio (excess pore water pressure normalized by the initial effective confining pressure) is a function of the strain amplitude and the number of cycles. He replaced the number of cycles N by the strain history ξ, which provides the possibility to generalize the constant strain condition into the irregular strain histories. A damage parameter k is used to represent the two variables (eq.3.9).

$$k = \xi e^{4.99\gamma} \tag{3.9}$$

with ξ= length of strain path= 4Nγc, for constant amplitude cycles.

$$\frac{\partial u}{\partial \sigma'} = G(k) = \left(\frac{A}{B}\right)\ln(1 + Bk) \tag{3.10}$$

with A=111.50, B=452.46.

3.3.3 Ishibashi's model (stress-controlled)

The pore pressure prediction model reported by Ishibashi (1977) is one of the most commonly used models. He analyzed the residual pore pressure at the end of each cycle and obtained the normalized incremental residual pore pressure (the difference between the normalized pore pressure in N[th] cycle and N-1th cycle) from a product of the stress history H, the number of cycle effects $\bar{N}$, and applied shear stress function I as is shown in equation 3.11:

$$\Delta U_N^* = H\bar{N}I \tag{3.11}$$

and can be represented as four material parameters:

$$\Delta U_N^* = (1 - U_{N-1}^*) \cdot \left(\frac{C_1 \cdot N}{N^{C_2} - C_3}\right) \cdot \left(\frac{\tau_{\theta z(N)}}{\sigma_{N-1}}\right)^n \tag{3.12}$$

C1, C2, C3, and n are four constant parameters. For the best fit, C1, C2, C3, and n equal to

6.13, 1,77, 0.46, and2.4, respectively.

3.3.4 Seed et al.'s model (stress-controlled)

Seed et al. (1976) presents an empirical formula to evaluate pore pressure

generation. The model only needs one criterion as the number of constant stress cycles to

obtain a condition of liquefaction.

$$r_u = \frac{1}{2} + \frac{1}{\pi} \arcsin\left(2\left(\frac{N}{N_L}\right)^{\frac{1}{\alpha}} - 1\right) \tag{3.13}$$

r_u is the pore pressure ratio, N_L is the number of cycles required to initiate the liquefaction

of the soil mass. α is a constant value based on the soil type and test condition with an

average value of 0.7.

3.4 Stress-Strain Behavior of Soils

In recent decades, many constitutive models have been developed to simulate the

soil stress-strain behavior under specific loading conditions. However, the actual behaviors

of soils are complicated and usually depend on many factors such as density, water content,

drainage conditions, stress history. (Duncan and Chang, 1970) The constitutive models are

either derived from experimental data or analytical deduction, and each model is only

applicable to the specific aspect of the soil behavior. The nonlinear elastic models are most

commonly used in the analysis of soil behaviors under cyclic loadings.

3.4.1 Linear elastic models

Although soil behaviors are non-linear, the isotropic soils can be regarded as linear elasticity in small strains. The elastic theory assumes the direction of the incremental stress is the same as the incremental strain and neglects the relations between the normal strains and shear stresses. (Potts, 1999) Only two independent parameters are necessary to represent the elastic soil behavior: E, young's modulus, and u Poisson's ratio. The relationship can also be shown as eq.3.14 in terms of G, elastic shear modulus, and K', effective bulk modulus. For linear elasticity, the shear modulus G is constant.

$$
\begin{Bmatrix} \Delta\sigma_x' \\ \Delta\sigma_y' \\ \Delta\sigma_z' \\ \Delta\tau_{xz}' \\ \Delta\tau_{yz}' \\ \Delta\tau_{xy}' \end{Bmatrix} = \begin{bmatrix} K'+4/3G & K'-2/3G & K'-2/3G & 0 & 0 & 0 \\ K'-2/3G & K'+4/3G & K'-2/3G & 0 & 0 & 0 \\ K'-2/3G & K'-2/3G & K'+4/3G & 0 & 0 & 0 \\ 0 & 0 & 0 & G & 0 & 0 \\ 0 & 0 & 0 & 0 & G & 0 \\ 0 & 0 & 0 & 0 & 0 & G \end{bmatrix} \begin{Bmatrix} \Delta\varepsilon_x \\ \Delta\varepsilon_y \\ \Delta\varepsilon_z \\ \Delta\gamma_{xz} \\ \Delta\gamma_{yz} \\ \Delta\gamma_{xy} \end{Bmatrix} \tag{3.14}
$$

$$
G = E'/2(1+\mu') \ ; \ K' = E'/3(1-2\mu') \tag{3.15}
$$

3.4.2 Non-linear elastic models

For large strains, the linear elastic models are not applicable, and in order to improve the simple model, the first step is to make the soil parameters stress or strain-dependent. Non-linear elastic models are most frequently used in the field of soil dynamics. Among those, hyperbolic models work well considering the advantage of computational simplicity as well as adequately reflecting the dynamic shearing behavior of soils (Cao, et al. 2014, Allani and Holeyman 2013, Shahnazari et al. 2010, Ansal 1987). The original model brought up by Kondner (1963):

$$
\sigma_1 - \sigma_3 = \frac{\varepsilon}{a + b\varepsilon} \tag{3.16}
$$

where σ_1 and σ_3 are major and minor principal stresses respectively, ε is the axial strain, and a and b are material constants determined by the undrained compression tests. As shown in figure 10. a is the reciprocal of the initial tangent modulus E_i, and b is the reciprocal of the asymptotic value of deviatoric stress $(\sigma_1-\sigma_3)_{ult,}$ which the stress-strain curve approaches at the infinite strain.
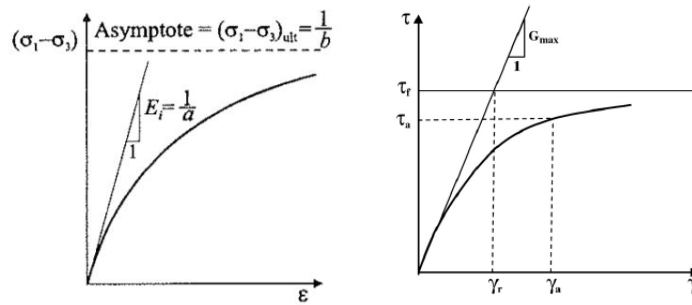
Figure 10 Hyperbolic stress-strain curve

At the same year, Kondner and Zelasco (1963) proposed the hyperbolic formula for shear stress-strain behaviors:

$$\tau = \frac{G_{max}\gamma}{1 + |\gamma/\gamma_r|} \tag{3.17}$$

where τ=shear stress, γ=shear strain, γ_r=reference shear strain, Gmax=initial shear modulus.

Duncan and Chang (1970) developed the hyperbolic model to be more applicable to triaxial test behavior. The Duncan-Chang model is based on the Mohr-Coulomb failure criteria, considering which the elastic modulus of the D-C model in loading condition, E_t, can be written as:

28

$$E_t = K_e P_a \left(\frac{\sigma_3}{P_a}\right)^n \left(1 - \frac{R_f(1 - \sin\varphi)(\sigma_1 - \sigma_3)}{2c\cos\varphi - 2\sigma_1\sin\varphi}\right)^2 \qquad (3.18)$$

K_e is the modulus number, n is the modulus exponent, the values of K_e and n can be

obtained from the plotting of initial elastic modulus E_i against σ_3 on a log-log scale from a

series of tests, where K is the intercept, and n is the slope of the straight line. P_a is

atmospheric pressure, which is used to normalize stress inputs. D-C model is widely

accepted as its soil parameters are easy to obtain from the triaxial tests.

3.4.3 Elastic-plastic Models

The elastic-plastic models induced the concept of plasticity, which can realistically

simulate real soil behavior. Initial, the soil behaves elastically. Once the yield stress is

reached, the soil starts to behave plastic. There are three types of plastic behaviors:

perfectly plastic, hardening plastic and softening plastic, as shown in figure 11.

(a) perfectly plastic   (b) softening plastic   (c) hardening plastic
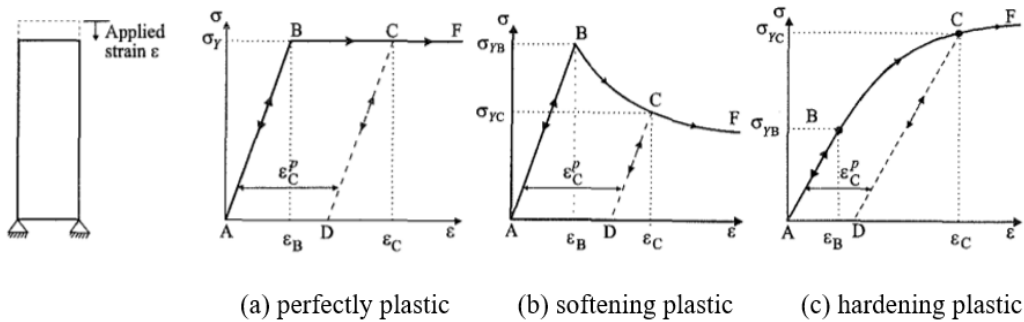
Figure 11 One-dimensional plastic behaviors under uniaxial loading

29

CHAPTER IV

WAVE ANALYSIS AND STIFFNESS DEGRADATION MODEL

4.1 Introduction

As mentioned in the first chapter, the one-dimensional problem can be considered as an analysis of the dynamic behavior of a cylinder embedded in a semi-infinite medium. Based on Novak's approximate analytical approach (1974), a one-dimensional finite-difference wave propagation model is programmed. The assumption is that the soils near the pile shaft are composed of a series of horizontal strips that extend to infinity. The strips are independent of each other. Besides the assumption by Novak's approach, there are some other assumptions made to analyze the problem:

- The pile is rigid, and no compression occurs during vibration.

- The motion of the pile and hammer is purely vertical without considering the horizontal vibration.

- The soil is homogeneous and isotropic.

- The pore pressure generated at the tip is the same as that at the shaft for the soil at the same depth.

- The movement of the pile is equal to the movement of the soil near the pile.
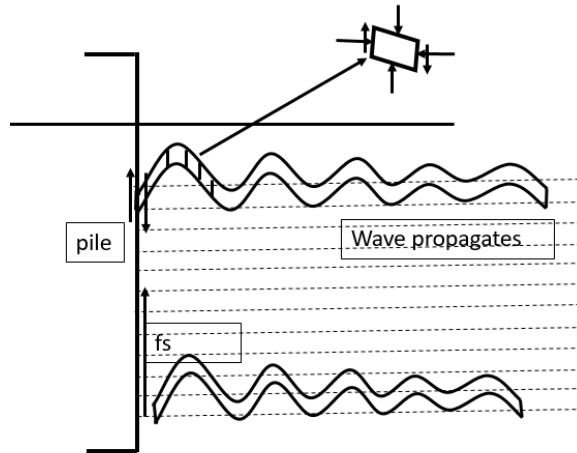
Figure 12 1-D approximate analysis

In this chapter, the program written to study the soil strength degradation, as well as the vibratory pile penetration in saturated sands, is introduced in detail.

Section 4.2 illustrates the finite difference model and the boundary conditions based on the 1-D wave equation.

Section 4.3 presents the constitutive model of soil behavior, the pore water pressure model, and the softening calculation used in the analysis.

Section 4.4 describes the model for a strip at the specific depth and the integration of single strips.

4.2 FD Wave Propagation Model

4.2.1 Implicit Finite Difference Model

The finite difference method is a relatively sophisticated numerical method with an intuitionistic mathematical concept and simple expression. In this method, the solution domain is divided into differential grids, and the continuous solution domain is replaced by finite grid nodes.

31

As mentioned before, the surrounding soil can be considered as axisymmetric. The shear stress can be written as:

$$\tau_{rz} = G\gamma \tag{4.1}$$

where G is the shear modulus, γ is the shear strain:

$$\gamma = \frac{\partial u_z}{\partial r} \tag{4.2}$$

u_z is the vertical displacement. Therefore, the shear stress can be written as:

$$\tau_{rz} = G\frac{\partial u_z}{\partial r} \tag{4.3}$$

the shear modulus, G, is a function of radial distance from the pile, G(r), during the process of vibration. And if we take a derivative of τ_{rz} concerning r:

$$\frac{\partial \tau_{rz}}{\partial r} = G\frac{\partial^2 u_z}{\partial t^2} + \frac{\partial u_z}{\partial r}\frac{\partial G}{\partial r} \tag{4.4}$$

From the equilibrium equation:

$$\frac{\partial \tau_{rz}}{\partial r} + \frac{\tau_{rz}}{r} = \rho\frac{\partial^2 u_z}{\partial t^2} \tag{4.5}$$

Combine (4.4) and (4.5), and then divided both sides by G:

$$\frac{\partial^2 u_z}{\partial r^2} + \frac{\partial u_z}{\partial r}\left(\frac{1}{G}\frac{\partial G}{\partial r}\right) + \frac{1}{r}\frac{\partial u_z}{\partial r} = \frac{\rho}{G}\frac{\partial^2 u_z}{\partial t^2} \tag{4.5}$$

Based on Taylor Expansion, the first and second-order differential equations are transformed into difference equations:

$$\frac{\partial^2 u_z}{\partial r^2} \approx (u_{i-1} - 2u_i + u_{i+1})/\Delta r^2 \tag{4.6}$$

$$\frac{\partial u_z}{\partial r} \approx (-u_{i-1} + u_{i+1})/2\Delta r \tag{4.7}$$

The left side of (4.5) which is the spatial derivative can be written as:

$$u_{i-1}\left[\left(\frac{1}{\Delta r^2}-\frac{1}{2r\Delta r}\right)+\left(\frac{-1}{2\Delta r}\frac{dlnG}{dr}\right)\right]+u_i\left(\frac{-2}{\Delta r^2}\right)+u_{i+1}\left[\left(\frac{1}{\Delta r^2}+\frac{1}{2r\Delta r}\right)+\left(\frac{1}{2\Delta r}\frac{dlnG}{dr}\right)\right]\ (4.8)$$

The spatial stiffness matrix [k $_{spatial}$] can be constructed from the coefficients of [u].

Combine (3.6), (4.5) and (4.8), and take the second time derivative for the right side of

(4.5), the whole equation is given by:

$$v_s{}^2\left(\frac{\partial^2 u_z}{\partial r^2}+\frac{1}{r}\frac{\partial u_z}{\partial r}\right)_i=\frac{u_i{}^{k+1}-2u_i{}^k+u_i{}^{k-1}}{\Delta t^2} \tag{4.9}$$

where $u_i{}^{k+1}$ is the displacement of point i at time t+Δt, $u_i{}^k$ is the displacement of point i

at time t, $u_n{}^{k-1}$ is the displacement of point i at time t-Δt, v_s is the shear wave velocity. Δt

is the time increment.

The right side of the equation is a time-domain finite difference equation, based on

the implicit approach, (4.9) can be transformed into the matrix form:

$$\{v_s{}^2\Delta t^2[k_{spatial}]-[I]\}[u]_{t+\Delta t}=-2[u]_t+[u]_{t-\Delta t} \tag{4.10}$$

If $\{v_s{}^2\Delta t^2[k_{spatial}]-[I]\}$ is represented by another stiffness matrix $[k_{comp}]$ and

$-2[u]_t+[u]_{t-\Delta t}$ is represented by a load vector [R] the formula can be more intuitively

expressed as:

$$[k_{comp}][u]_{t+\Delta t}=[R] \tag{4.11}$$

33

4.2.2 Boundary conditions

Pile shaft boundary condition

In the present study, the governing boundary condition should be kinemetric (i.e., displacement)rather than dynamic (i.e., stress). Because the shear stress is relatively small to resist the pile movement, the vibratory behavior is not strongly influenced by the soil resistance (Holeyman, 1997). Therefore, the displacement boundary near the pile shaft is presented as:

$$U_b = U_{bamp} \sin \omega t \qquad (4.12)$$

The boundary displacement amplitude U_{bamp} of the soil near the pile is equal to the displacement of every pile element. Because the pile is assumed to be rigid, the displacement of every pile element is the same as the pile amplitude, which can be obtained from eq. (2.6).

Far-field boundary condition

Theoretically, the shear wave away from the vibratory pile propagates to infinity, while the existence of radiation damping dissipates the energy of the wave. This makes the wave energy decrease and disappears in far-field. Due to the finite length of the domain in numerical analysis, the far-field boundary must be formulated to avoid spurious reflection of waves. The can be achieved using the following equivalent viscous boundary:

$$\tau = \frac{G}{v_s} \frac{\partial u}{\partial t} \qquad (4.13)$$

where $\frac{G}{v_s}$ is the equivalent viscosity to absorb a wave impacting the far-field boundary. This leads to:

$$G\frac{\partial u}{\partial r} = -\frac{G}{v_s}\frac{\partial u}{\partial t} \tag{4.14}$$

We take the time and spatial difference equation for both sides respectively, n is the number of points in radial direction:

$$\frac{u_n{}^{k+1} - u_{n-1}{}^{k+1}}{\Delta r} = -\frac{1}{v_s}\frac{u_n{}^{k+1} - u_n{}^{k}}{\Delta t} \tag{4.15}$$

The boundary condition can be expressed by:

$$(1 + A)[u_n]_{t+\Delta t} - [u_{n-1}]_{t+\Delta t} = A[u_n]_t \tag{4.16}$$

A is a constant value given by:

$$A = \Delta r/v_s\Delta t \tag{4.17}$$

4.3 Soil and Pore Pressure Models

4.3.1 Constitutive Model

The constitutive relationship selected for this study is capable of simulating both nonlinear and cyclic behavior. Namely, a hyperbolic model was selected based on considerations of computational simplicity while still adequately reflecting the shearing behavior of soils (Cao, et al. 2014, Allani and Holeyman 2013, Shahnazari et al. 2010, Ansal 1987).

As is shown in fig. 13 from Vucetic's experimental results (1993; 1994), the secant shear modulus (G_t) decreases with the shear strain during every monotonic loading, and the initial shear modulus (G_{max}) decreases with the number of cycles.
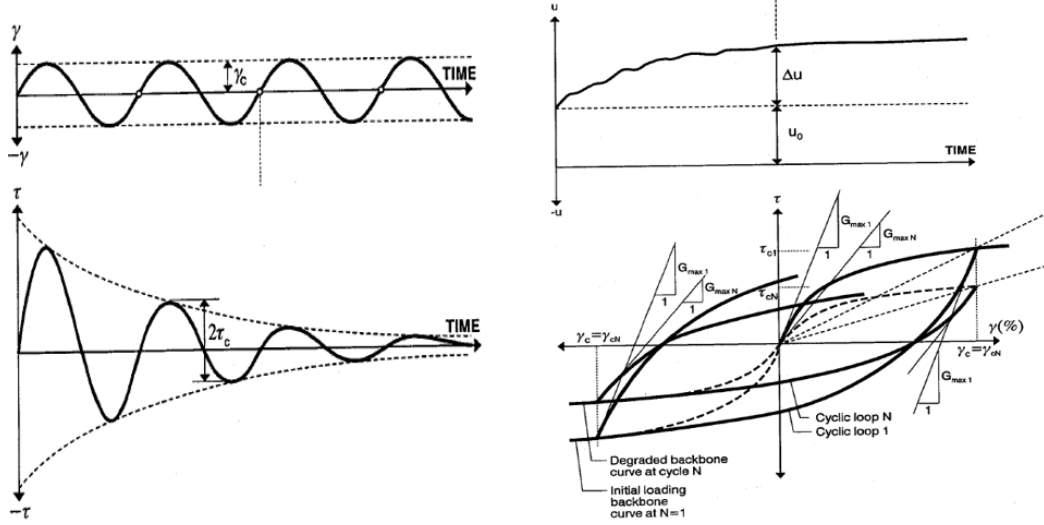
Figure 13 Soil behavior under cyclic shear strain amplitude loading (Vucetic, 1993; 1994)

The initial monotonic loading is referred to as the backbone curve, which is the basis to generate other unload-revise load curves. The backbone curve (Kondner, 1963) is given by:

$$\tau/\tau_{max} = \delta/(\delta + 1) \, with \, \delta = \gamma/\gamma_r = \gamma * G_{max}/\tau_{max} \tag{4.18}$$

The unload-revise load curve is described by (Masing, 1926):

$$\tau - \tau_0 = (\gamma - \gamma_0)/(1/G_{max} + (\gamma - \gamma_0)/2\tau_{max}) \tag{4.19}$$

If we take the derivatives of both sides with respect to $(\gamma - \gamma_0)$:

$$\frac{d(\tau - \tau_0)}{d(\gamma - \gamma_0)} = \left(\frac{1}{G_{max}} + \frac{(\gamma - \gamma_0)}{2\tau_{max}}\right)^{-1} - \frac{(\gamma - \gamma_0)}{2\tau_{max}}\left(\frac{1}{G_{max}} + \frac{(\gamma - \gamma_0)}{2\tau_{max}}\right)^{-2} \tag{4.20}$$

From the definition of tangent shear modulus:

$$G_t = \frac{d(\tau - \tau_0)}{d(\gamma - \gamma_0)} \tag{4.21}$$

36

The secant shear modulus can be expressed as:

$$G_t = \left(\frac{1}{G_{max}} + \delta\right)^{-1} - \delta\left(\frac{1}{G_{max}} + \delta\right)^{-2} \quad with \delta = \frac{(\gamma - \gamma_0)}{2\tau_{max}} \tag{4.22}$$

The secant shear modulus is calculated by two main parameters: G_{max} and τ_{max}. The initial shear modulus and ultimate shear stress for the first cyclic loading are inputs from the CPT test. And are updated in every cycle based on the excess pore pressure.

4.3.2 Pore Pressure Generation Model

According to Dobry (1982), the rate of excess pore water generation increases with the decrease of relative density as well as the increasing strain level. The pore pressure generation model used in this study based on the experimental results of Dobry (1982).

The pore pressure ratio under various cyclic shear strains and the number of cycles for loose, mid dense, and dense sands are plotted in fig.14-16, respectively. The sand is Monterey No. 0 Sand with relative density Dr=45% for loose sands, 60% for medium dense sands, and 80% for dense sands. By comparing the three curves, it is obvious that for a specific shear strain, the pore pressure generates fastest in the loosest sands and slowest in the densest sands.

Based on Hardin and Drnevich's equation (4.23), the shear modulus of the sand can be calculated as 90Mpa. From the curves, the threshold strain γ_{cv}=0.02%, which is independent of relative density. Beyond the threshold strain, the pore pressure increases rapidly.

$$G_{max} = 1230 \frac{(2.973 - e)^2}{1 + e} (\sigma_3')^{1/2} \tag{4.23}$$

As shown in fig.17, the relationships between pore pressure ratio and cycle number in log scale are approximately linear. As a result, the curves in fig. 14-16 are interpolated both in log scale with respect to strain amplitude and number cycles, respectively.
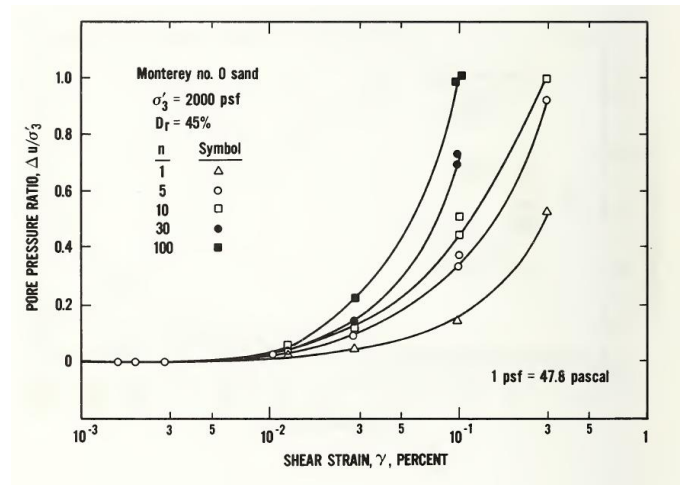
Figure 14 Build-up of residual pore pressure as a function of cyclic strain for loose Monterey Sand (Dobry et al, 1982)
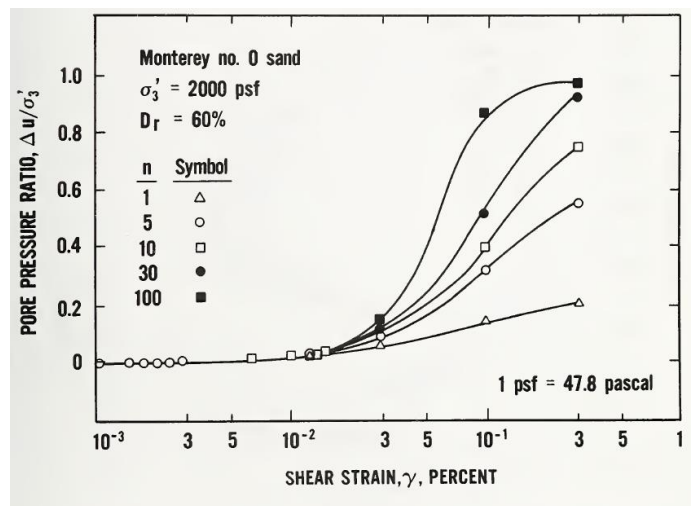
Figure 15 Build-up of residual pore pressure as a function of cyclic strain for medium dense Monterey Sand (Dobry et al, 1982)
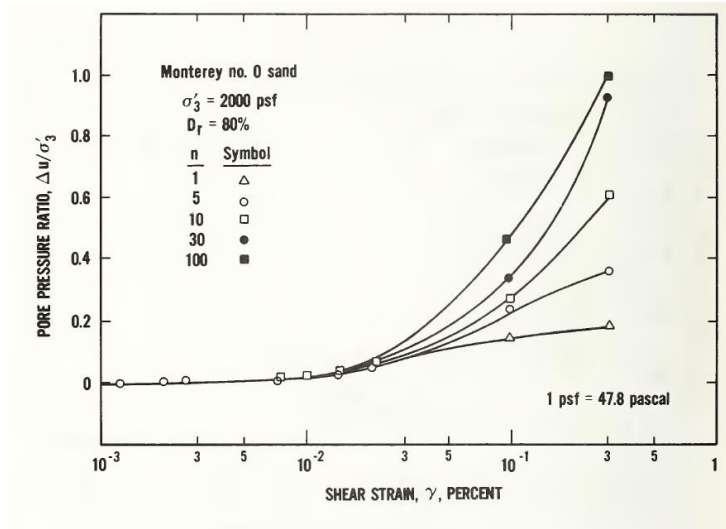
Figure 16 Build-up of residual pore pressure as a function of cyclic strain for dense Monterey Sand (Dobry et al, 1982)
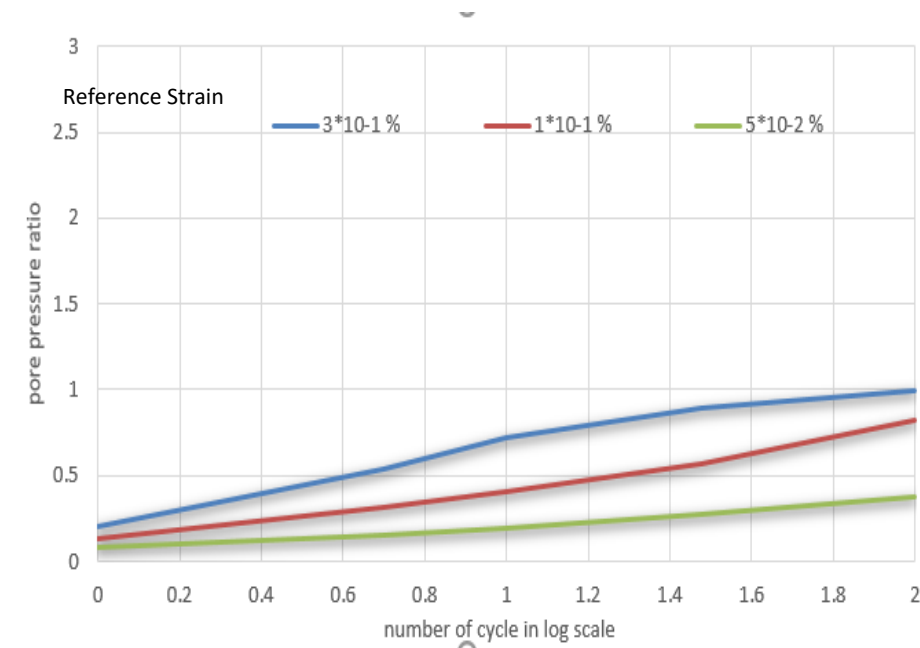
Figure 17 Plots of pore pressure ratio vs. log(N) for different strain amplitudes

The effective overburden stress and the initial shear modulus for every cycle decrease with the raising of excess pore water, the process follows eq. (4.24) and (4.25), which can be deducted from (4.23):

$$G_{max1} = G_{max0} \left(\frac{\sigma'}{\sigma'_0} \right)^{1/2} \tag{4.24}$$

$$\tau_{max1} = \tau_{max0} \left(\frac{\sigma'}{\sigma'_0} \right) \tag{4.25}$$

The static initial shear modulus ($G_{max,N=1}$) and the static ultimate shear stress ($\tau_{max,N=1}$) are based on the CPT data (cone resistance q_c, local skin friction f_s, and friction ratio FR), and their relationship suggested (Holeyman, 1997):

$$G_{max0} = K * q_c, \qquad with \ \ K = 15 \tag{4.26}$$

$$\tau_{max0} = \beta * f_s, with \ \ \beta = 0.65 + 0.35 * tanh1.5(FR - 2\%) \tag{4.27}$$

4.4 Technique Route and the Integrated Model

All the component models used in the strip model are described in detail. A summary of the technical route for the strip model is presented in fig. 18. This model simulates the excess pore pressure accumulation as well as skin friction degradation for a single strip with a thickness of 1m at a specific depth. The shaft friction along the pile is calculated by integrating the friction resistance from the ground to the penetration depth (eq.4.28).

$$F_{shaft} = \sum_{z=0}^{z=depth} (f_{inner,z} * 2\pi r_{inner} dz + f_{outer,z} * 2\pi r_{outer} dz) \tag{4.28}$$

With the assumption that the excess pore pressure level at the tip is the same as that at the shaft, the tip resistance can be approximately calculated as:

$$F_{tip} = k_c * q_c * \left(1 - \frac{\Delta u}{\sigma'}\right) * A_{tip} \tag{4.29}$$

where k_c is a factor estimated as 0.25.(Briaud, 2013) A_{tip} is the area of the pile tip. Δu is the excess pore pressure.

As mentioned before, the total driven force equals the sum of the weight of vibration parts and the driven force from the hammer. The total resistance force equals the sum of the tip resistance and the shaft friction. The total resistance decreases during the vibration of the pile, and when the total resistance is lower than the total driven force, the pile penetrates.
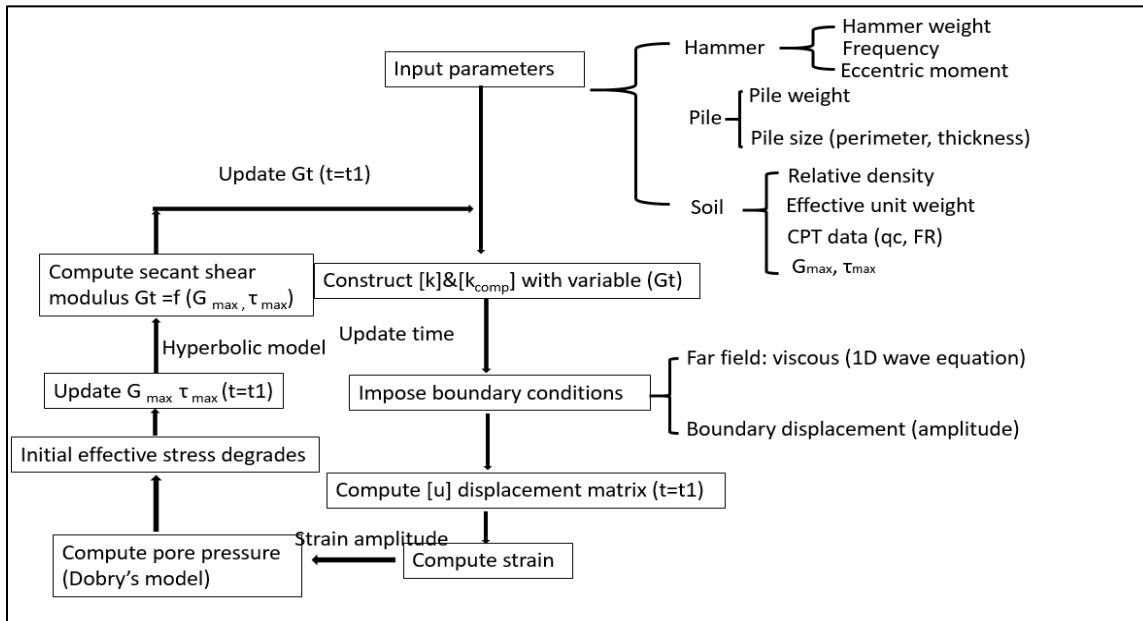
Figure 18 Technique route of the strip penetration model

4.5 Penetration Time Analysis

In this study, we assume that when the total driving force is greater than the total resistance, the pile will penetrate in an increment of one meter. However, even in a very weak soil layer, the pile does not undergo a free fall. Rather, the pile is supported by the clamping device with a maximum speed of movement. Therefore, the penetration consists of two parts: the critical time and the basic time. The critical time is the time required to reduce the total resistance to a force that equals the driving force (Fig. 19).
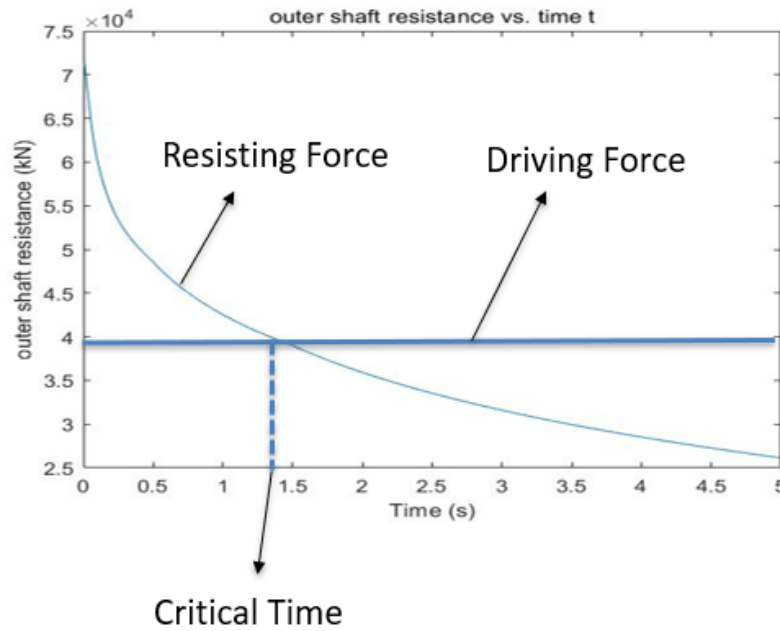
Figure 19 Reduction of shaft resistance vs. time

The basic time is the shortest time needed for the pile to move one meter, that is, when the soil layer is very weak (the resistance before vibration is less than the driving force), the time needed for the pile to penetrate one meter. The largest movement of the pile for every cycle is equal to the amplitude. The time period for every cycle is the reciprocal of the frequency. And the basic time for one-meter penetration can be calculated by eq.4.30.

When the pile encounters a stiff layer, it requires additional time to vibrate and weaken the soil. That part is the critical time as we mentioned in the previous paragraph.

$$t_{basic} = \frac{1000}{Amplitude(mm)} * \frac{1}{f} \qquad (4.30)$$

The penetration time is the sum of the basic time and the critical time, considering the time needed for both movement and stiffness reduction. For the very soft layers, the critical time is zero and the penetration time equals the basic time.

CHAPTER V

CASE STUDY

In this chapter, the cases of a large steel monopile and a small sheet pile are analyzed respectively. The parameters of piles and hammers, and the soil profiles are reported by Dorp (2019) and Viking (2002) and are input into the WASD model to simulate the penetration process and compute the penetration time. Then the accuracy of the model is checked by comparing the predicted penetration time with the actual penetration time.

5.1 Case One: A Steel Monopile (Open-ended)

5.1.1 Input parameters

Pile-hammer parameters

According to Dorp, et al. (2019), the pile and hammer parameters are shown in Table. 4. According to eq. (5.1) and (5.2), the total driving force is 6.8MN, the weight of the dynamic part is 1.8MN, and the dynamic force is about 5MN. The frequency of vibration and eccentric moment largely determines the driving force. From (5.3), the amplitude of pile-hammer vibration is 1.8mm.

$$Fc = \text{Mecc} * \omega^2 \tag{5.1}$$

$$F_{driving} = F_c + W_{dynamic} \tag{5.2}$$

$$A = \frac{M_{ecc}}{m_{dynamic}} \tag{5.3}$$

Table 4 Pile-hammer parameters from Dorp (2019)

Pile Diameter (m)	Pile thickness (mm)	Pile weight (tons)	Pile length (m)	Vibrator dyn. Mass (tons)	Eccentric moment (kg.m)	Frequency (Hz)
4	46	126	27	54	320	20

Soil parameters

The soil profile based on the CPT test is shown in Fig.20. The cone resistance qc is discretized as the blue line shows. The friction ratio is 1%. The effective unit weight of soil is 8.2 kN/m3, the density of soil is $1.84*10^3$ kg/m^3.
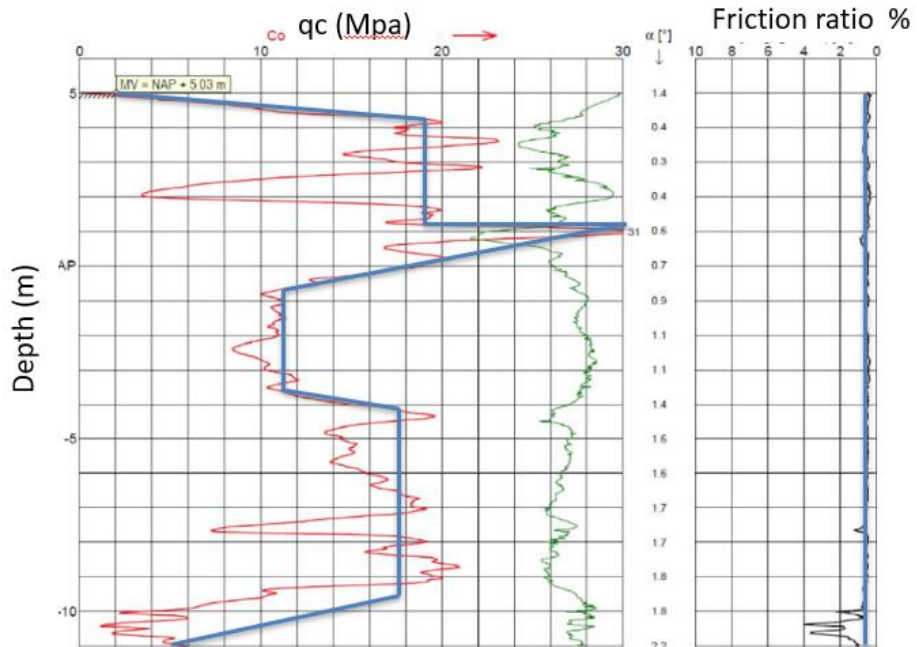
Figure 20 Cone resistance (left) and friction ratio (right) (Dorp, 2019)

Additional assumptions

Because the waves traveling between the inner walls of the pile are denser than those outward. The soil at the pile tip is more easily liquefied. We assume there is no plugging.

In addition, the penetration process is very fast, typically less than 5mins. The excess pore water pressure does not have enough time to dissipate, so we assume no dissipation occurs during penetration.

5.1.2 Pore pressure generation study for a single strip

The pore pressure generates very fast in the first several seconds. The pore pressure build-up during the process of vibration is regarded as that in a cyclic simple shear test. The waves propagating in soils are simulated and shown in Fig.21, from which the damping in the soil is manifest.
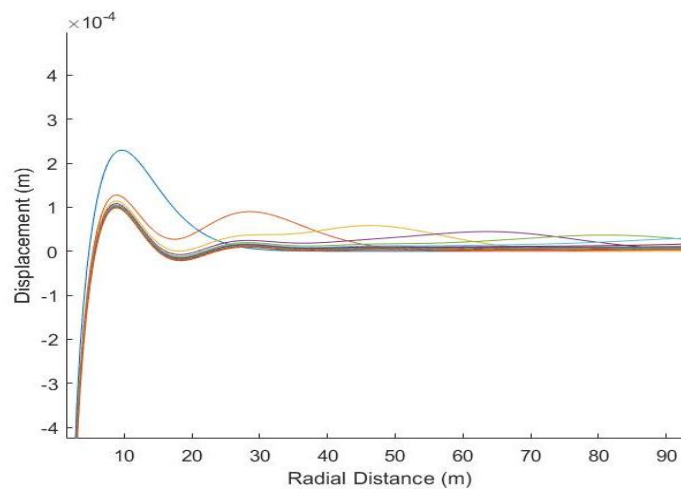
Figure 21 Shear wave propagation

The strain amplitude of the soil near the pile shaft is shown in Fig.22 as about 0.1%.

Pore pressure generation in the soil near shaft for 5 seconds is simulated at a depth of 10m

(Fig.23). After 5 seconds, the soil near the pile is approximately 80% liquefied ($\sigma' = \Delta u$).

Fig. 24 is the pore water generation distribution with the radial distance at t=5s at a depth

of 10m. From the figures, the influential radial distance is estimated as about 5m.
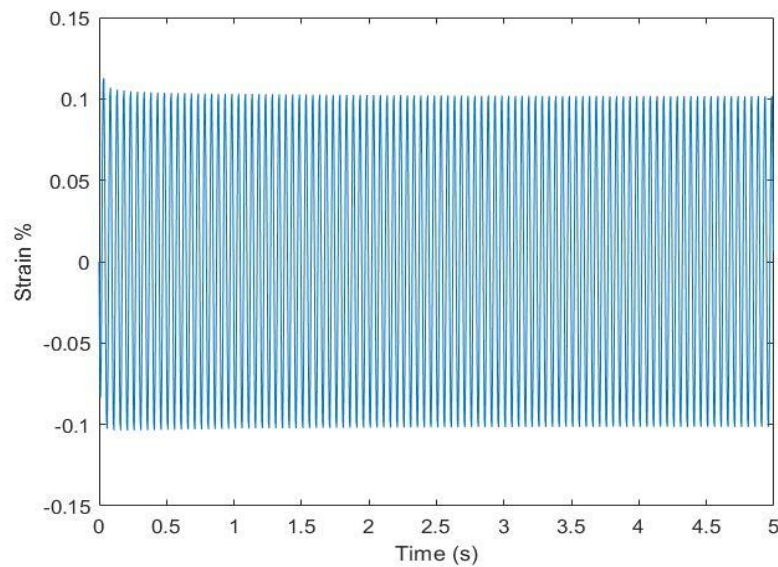
Figure 22 Strain amplitude
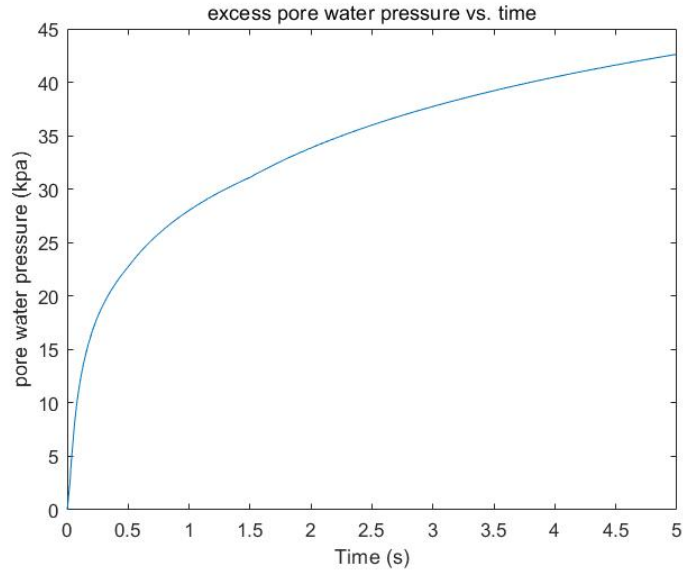
Figure 23 Pore pressure generation at shaft for 5 seconds (depth=10m)
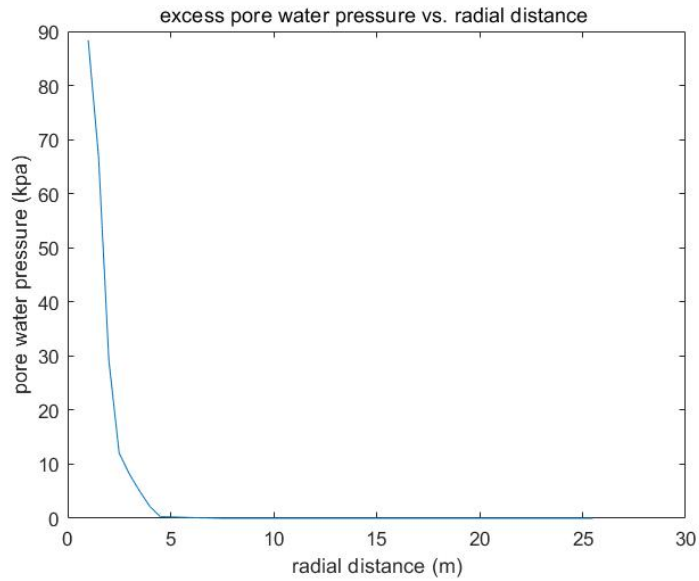
Figure 24 Pore pressure distribution with radial distance at t=5s (depth=10m)

5.1.3 Resistance Degradation for a single strip in Undrained Condition

The second set of simulations are for the pile embedded at a specific depth. The pile embedded 20m deep subjected to a cyclic force is analyzed as an example.

The frictional resistance along the 20m pile is reduced from 72MN to 26MN in 5seconds. For the first 10 cycles, the shaft resistance decreases very rapidly. As cyclic loading continues beyond 10 cycles, the rate of degradation in shaft resistance decreases. Beyond 100 cycles, the rate of degradation in shaft resistance becomes very small. This implies that most of the strength loss in the first 100 cycles, and the pile may fail to penetrate if it does not penetrate in the first several seconds.
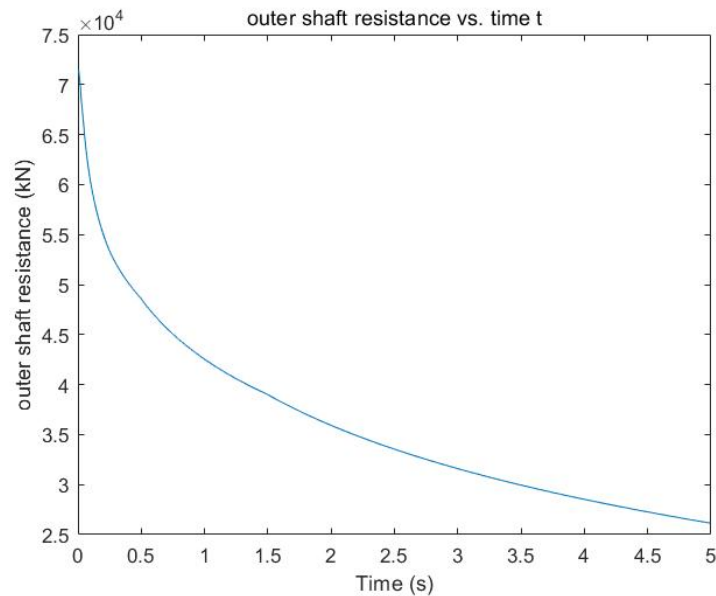
Figure 25 The degradation of the shaft resistance (depth=20m)

The tip resistance degradation at 20m is shown in Fig.26. Compared with the shaft friction resistance, the tip resistance is relatively low.

49
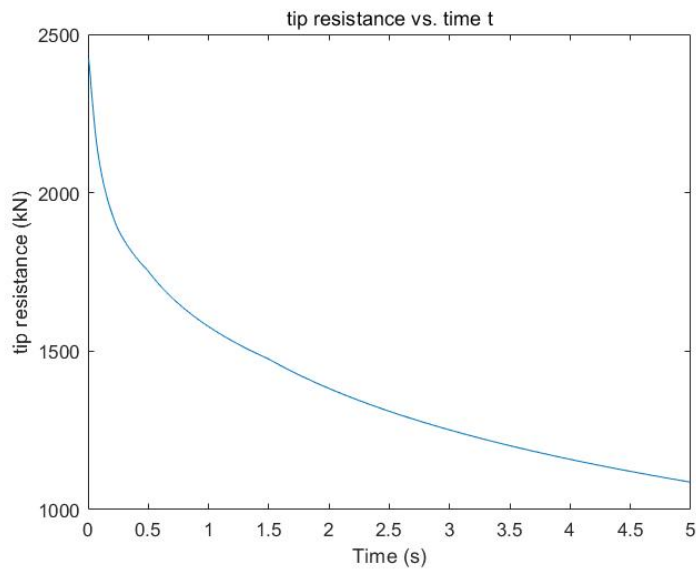
Figure 26 Tip resistance degradation at 20m

5.1.4 Comparison and Analysis of the Prediction Penetration Time

A comparison of the estimated and actual penetration speeds is shown in Figure 29. From the curve, we can see the stiff layer 3-4m underground is successfully reflected in the prediction speed by the WASD model. Nevertheless, the penetration speed for the whole driving process is overpredicted and a peak of speed at 11m is not shown in the prediction speed.

The deviation of prediction results can be explained in the following aspects: The absence of the peak penetration speed in a deeper stratum is due to the neglect of the corresponding weak stratum (low cone resistance value) in discretizing the CPT data. The overprediction is because the soils are partially saturated instead of fully saturated and the hard layer at 3m is dry sand (Dorp, 2019). There is no excess pore pressure generation in

the dry sand, and the pore pressure in the unsaturated sands is much lower than that in the saturated sands. In our prediction, we overpredicted the generation of pore pressure as well as the reduction of the resistance force. And thus, the deviation of the penetration times occurs.
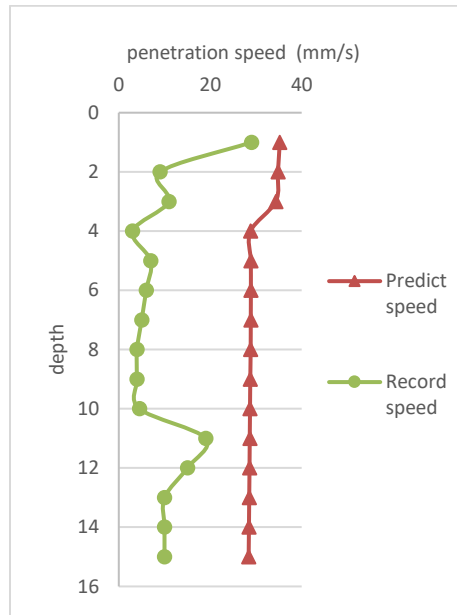
Figure 27 A comparison of the estimated and actual penetration speeds

5.2 Case Two: A Sheet Pile

5.2.1 Input parameters

The second full-scale field test reported were performed in Vårby, a suburb of Stockholm (Sweden). The test site was chosen firstly for its relatively homogeneous soil conditions, and secondly because there was a good probability of being able to keep the sensors in place for the entire duration of the planned field tests. (Viking, 2002)

Pile-hammer parameters

The second case is a sheet pile reported by Viking in 2002. The vibrator parameters and pile parameters are listed in table 5.

Table 5 Pile-hammer parameters by Viking (2002)

Vibrator parameters
Unbalanced moment, $M_e = 10$ kgm
Driving frequency, $f_d = 41$ Hz
Dynamic mass of the vibrator, $m_v = 2450$ kg
Pile parameters
One sheet pile without clutch friction
Section area, $A_t = 95.2$ cm^2
Sheet pile perimeter, $\chi = 150$ cm
Sheet pile length, $L = 14$ m
Mass of sheet pile, $m_p = \rho A_t L \sim 1010$ kg

Soil parameters

The results of the CPT test are shown in Fig.28. The water table is 2 meters below the ground. The left curve is the uncorrected cone resistance, the middle one is the sleeve friction and the right one is the friction ratio. The soil profile is interpreted from CPT tests and presented in table 7. Except for the first 2m of clays, all the layers are sand soils, which are the object soils of this study. The penetration depth of Viking's simulation (2002) is 12m, so the same penetration depth is used in this study.

Table 6 Soil profile of the second case (Axelsson, 2000)

Depth range [m]	Soil type
0 - 2.5	clay
2.5 - 4.5	silty sand
4.5 - 8	sand
8-14	silty sand
14 - 19	gravelly sand
19 - 24	silty sand
24 -	sand
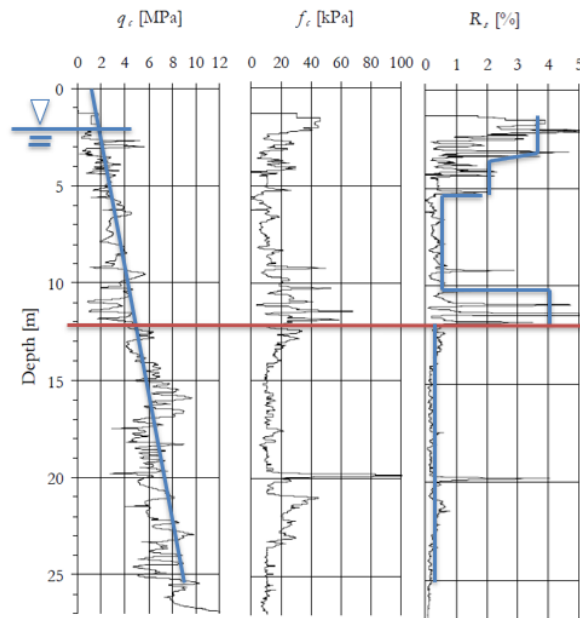
Figure 28 CPT results (Viking, 2002)

5.2.2 Comparison and Analysis of the Prediction Results

Figure 29 shows a comparison of predicted and actual penetration speed. The pink line is the actual penetration speed. The green line is the result of WASD's prediction. The blue line is the result of Viking's prediction by using Vipere. It can be seen from the figure that the WASD's prediction curve almost coincides with the actual curve, which indicates that the WASD model has successfully predicted the penetration rate of the vibratory pile in saturated sand and it even works much better than Vipere model used by Viking. The soil is soft and penetration speed is almost constant during the driving process. This also indirectly reveals that when the soil layer is soft, the basic speed determines the penetration speed. Figure 30 is the comparison of predicted and actual penetration time.
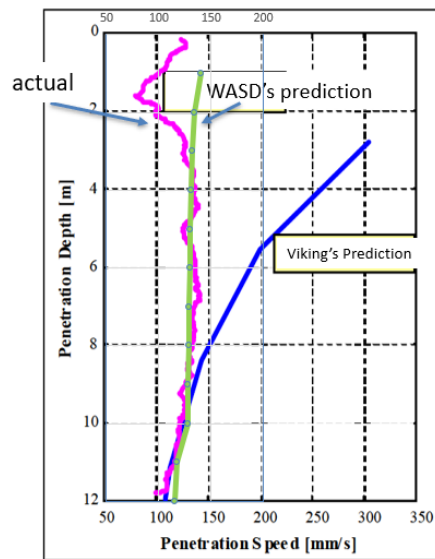
Figure 29 Comparison of predicted and actual penetration speed
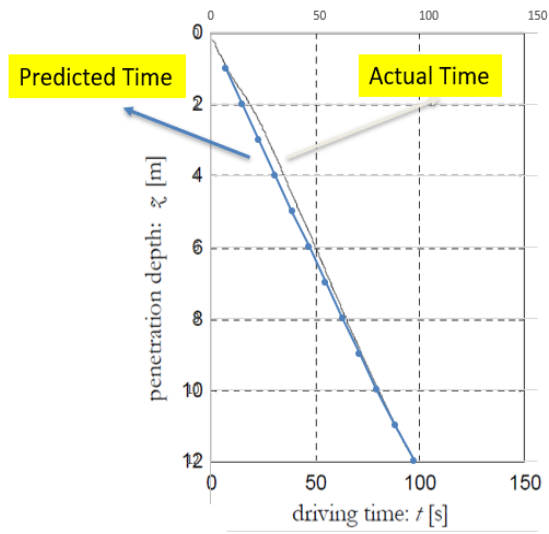
Figure 30 Comparison of predicted and actual penetration time

CHAPTER VI

PARAMETRIC STUDY

In this chapter, the influence of different pile-related and hammer-related parameters on penetration time is studied based on the open-ended steel pile in the first case study. The results show that the critical parameters such as the pile diameter, pile weight, hammer size, and vibration frequency have a great influence on the drivability.

Section 6.1 introduces the input parameters for the parametric studies. The soil profile used here is idealized linearly increasing.

Section 6.2 investigates the sensitivity of the prediction to the hammer-related parameter.

Section 6.3 uses a coefficient of correction to simulate the excess pore water dissipation during the driving process. And then the sensitivity analysis of the penetration time is conducted.

Section 6.4 illustrates the difference of the waves propagating inside and outside the pile, and then this section analyzes the sensitivity of the prediction to the internal friction.

6.1 Input Parameters

Pile-hammer parameters

The pile and hammer used in the parametric study are the same as those in the first case study (table 7).

Table 7 Pile and hammer parameters of the parametric study

Pile Diameter	Pile thickness	Pile weight	Pile length	Vibrator dyn.	Eccentric moment	Frequency
(m)	(mm)	(tons)	(m)	Mass (tons)	(kg.m)	(Hz)
4	46	126	27	54	320	20

Soil Profiles

The CPT parameter, q_c, is linearly increasing with depth as shown in Fig.31. The uncorrected cone resistance at the ground is 4.8Mpa, at 27m deep is 29.1Mpa. The friction ratio is 1%.
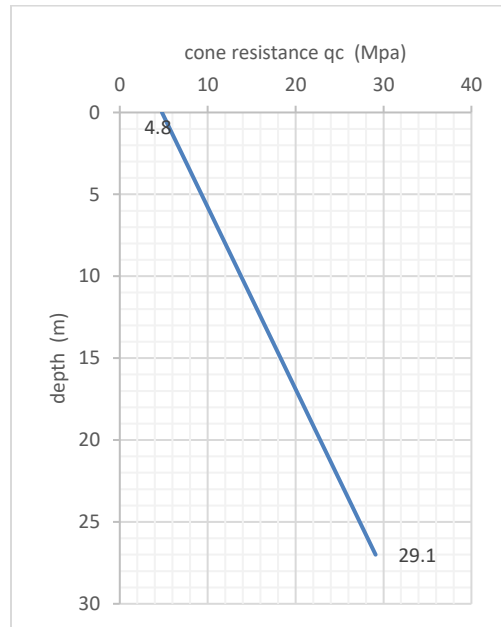
Figure 31 Uncorrected cone resistance

6.1 Sensitivity Analysis of Hammer-Related Parameters

6.1.1 Influence of Hammer Sizes

57

As mentioned in chapter 2, the selection of hammer sizes (weight& eccentric moment) influences the drivability of the pile. The eccentric moment is generally related to the weight of the hammer. The sizes of the four hammers are listed in table 5. Hammer 1 is the original hammer. Hammer 2 is twice the size of Hammer 1. Hammer 3 is half the size of Hammer 1and Hammer 4 is 0.8 times the size of Hammer 1.

Table 8 Sizes of four hammers

	Eccentric moment (m*s)	Weight of the hammer (ton)
Hammer 1	320	54
Hammer 2	640	119
Hammer 3	160	29
Hammer 4	260	44

The critical times for 27m pile driving by using four different hammers are plotted in Fig.32 as 120s, 14s, 674s, and 329s, respectively. Hammer 3 meets refusal at 19m. From these results, we can conclude that the penetration time, as well as the driving ability, is very sensitive to the size of the vibratory hammer. The penetration speeds for the four hammers are shown in Figure 33. The penetration speed increases with the size of hammers.
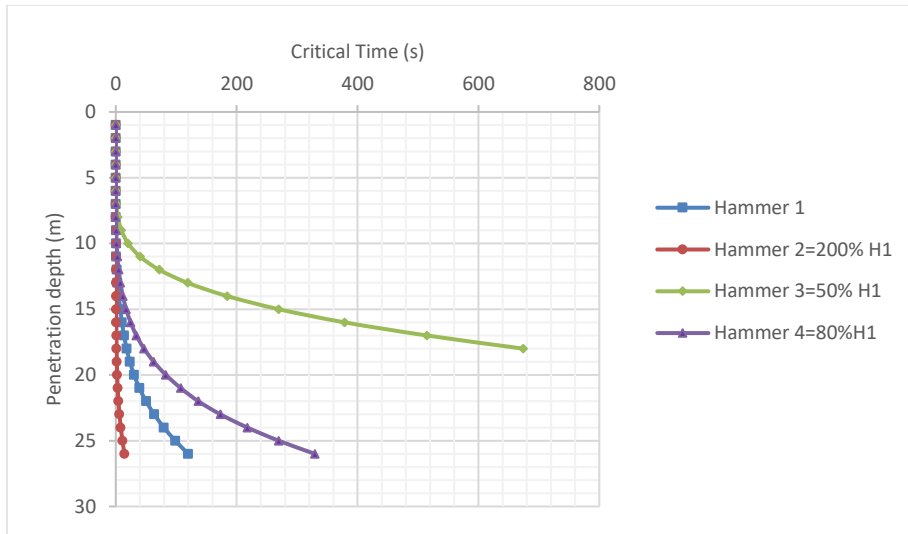
Figure 32 Critical times for different hammers
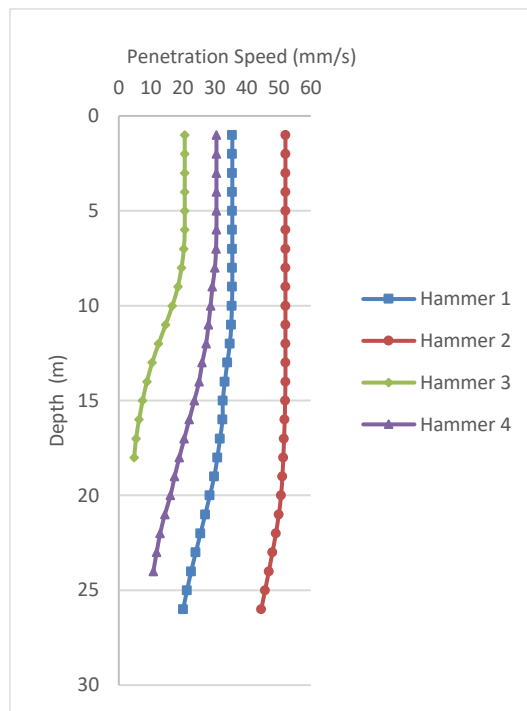
Figure 33 Penetration speeds for different hammers

59

6.1.2 Influence of Hammer Frequencies

As shown in equation 2.2, the vibration frequency determines the centrifugal force of the vibratory hammer. A comparison is made between hammers with three frequencies of 15Hz, 20Hz, and 25Hz. The critical times represented in Fig.34 for 27m driving are 500s, 120s, and 34s, respectively. The frequency decreases 5Hz, the responding penetration time increases 400%; and if the frequency increases 5Hz, the penetration speed is 300% faster. For the reason that the model does not simulate the resonance of the soil-pile system, the frequencies selected for the parametric study are below the resonant frequency of the soil-pile system.
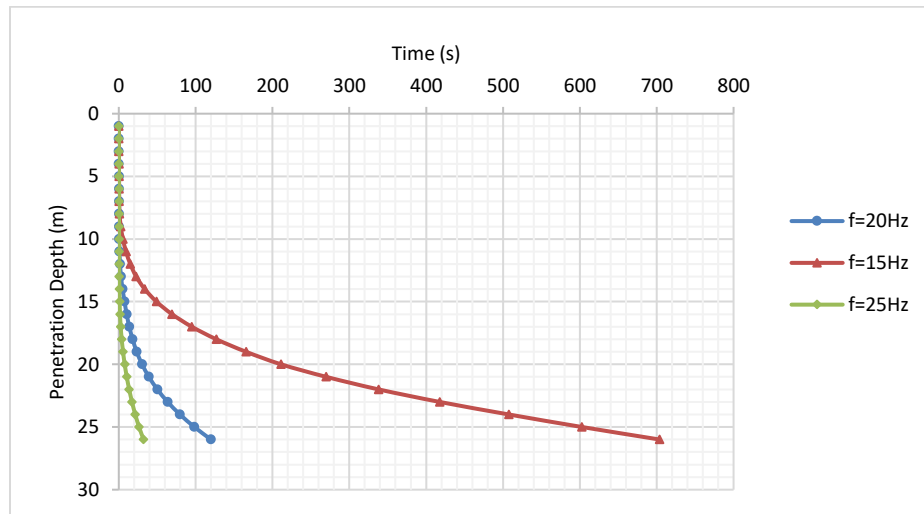
Figure 34 Critical times for different frequencies

6.2 Sensitivity Analysis of Pile-Related Parameters

6.2.1 Influence of wall thicknesses

The thickness of the pile wall determines the contact area between the pile tip and the soil, so it affects the resistance of the pile tip. At the same time, if the radius of the pile is fixed, the thicker the pile wall is, the smaller the internal diameter of the pile is, and the smaller the internal friction resistance is. Therefore, the increase of the wall thickness increases the tip resistance but decreases the inner friction resistance. The sensitivity analysis focuses on three piles with different wall thicknesses (Table 9). The pile lengths, diameters, and the unit weights are the same, the weight of each pile is calculated based on wall thickness.

The penetration time results of the three piles using the same hammer are shown in figure 35. For the 27-meter penetration, although the difference of penetration time is not great, we can still find that the thinner the pile wall is, the lighter the pile is, the corresponding driving force is smaller, but the penetration speed is faster because of the reduction of the tip resistance. It can also be seen that the thickness of the pipe wall has little effect on the side friction resistance and the tip resistance has little effect on the penetration speed.

Table 9 Different wall thicknesses of piles

	Pile length (m)	Diameter (m)	Thickness (mm)	Weight (t) (8.11ton/m3)
Pile1	27	4	46	126
Pile2	27	4	23	62
Pile3	27	4	34	93
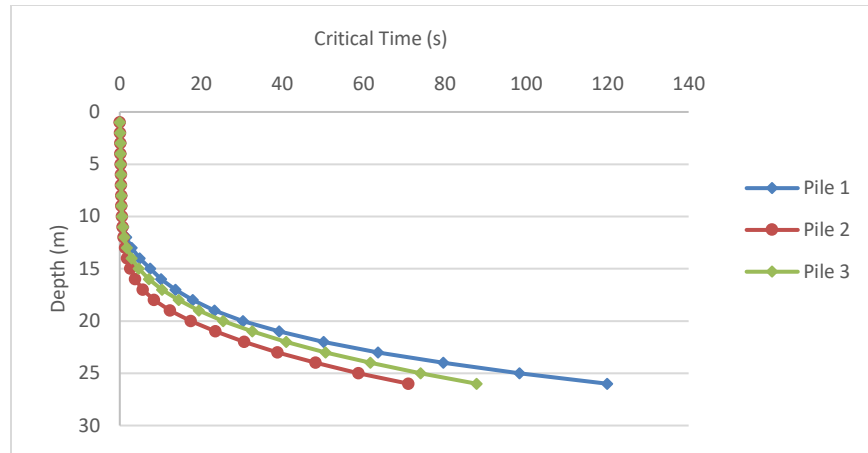
Figure 35 Prediction results of different pile thicknesses

6.2.2 Influence of pile diameters

For piles with the same length and wall thickness, the larger the diameter is, the heavier the pile will be, and the larger the driving force will be. At the same time, due to the increase in the contact area, the shaft and tip resistance are also much greater. A group of three piles with different diameters shown in table 10 are analyzed and the penetration times are plotted in figure 36. From the critical times during penetration, it can be found that the increase of the pile diameter causes a decrease in the pile drivability.

Table 10 Different diameters of piles

	Pile length (m)	Diameter (m)	Thickness (mm)	Weight (t) (8.11ton/m3)
Pile1	27	4	46	126
Pile4	27	3	46	94
Pile5	27	5	46	158
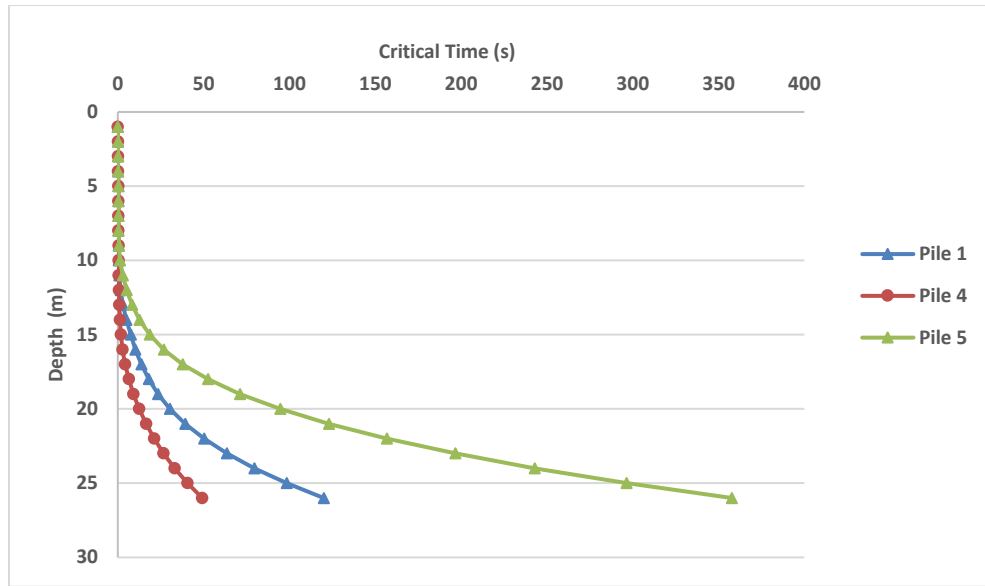
Figure 36 Prediction results of different pile diameters

6.2.3 Influence of pile lengths

For the piles with the same diameter and wall thickness, the length of the pile directly reflecting the weight of the pile. The pile parameters and the prediction results are shown in table 11 and figure 37, respectively. Two piles with a length of 27m and 54m are simulated to penetration 27m. The longer pile seems to have a lower driving capability and meet the refusal at 22m, even though it is twice as heavy as the other one. This might because from equation 6.1, the increase of the pile weight leads to a decrease of the vibration amplitude, and then a decrease of the pore pressure generation controlled by the strain amplitude.

$$\text{Amplitude} = \frac{Eccentric\ moment}{mass\ of\ vibrator + mass\ of\ pile} \tag{6.1}$$

Table 11 Different Lengths of Piles

	Pile length (m)	Diameter (m)	Thickness (mm)	Weight (t) (8.11ton/m3)
Pile1	27	4	46	126
Pile6	54	4	46	252
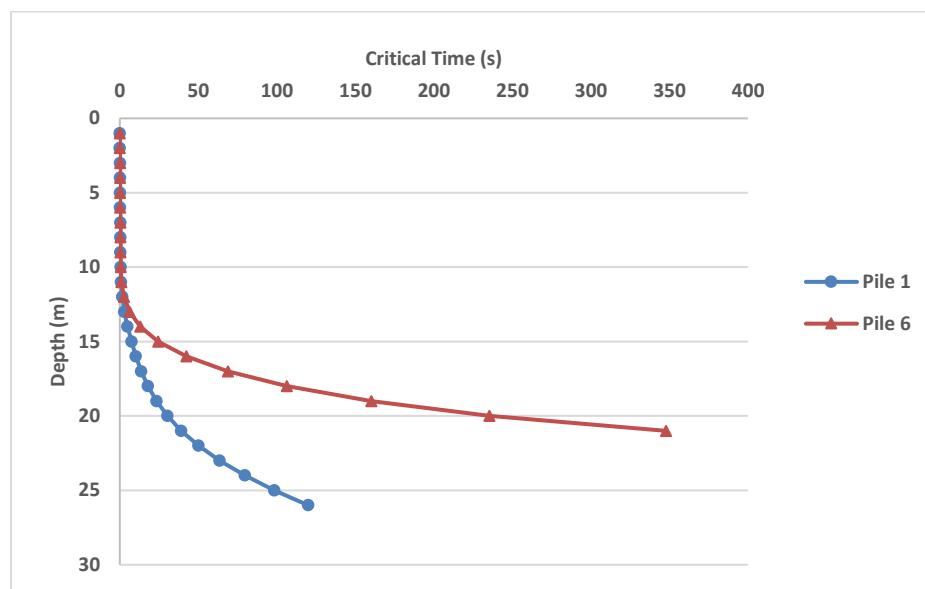
Figure 37 Prediction results of different pile lengths

6.3 Sensitivity Analysis of the Dissipation Factor

Chapter 5 has illustrated that this study is for undrained conditions without considering the pore water dissipation because of the fast penetration process. However, since the permeability of sands is relatively high, significant dissipation in excess pore pressure can occur concurrently with the pore pressure generation. If we crudely use a

64

dissipation factor to correct the excess pore water pressure instead of simply neglect it, we could investigate the sensitivity of the prediction results to the pore water dissipation.

Various dissipation factors are used to calculate the time for the penetration from the ground to 27m deep (Fig. 38). For 50% dissipation, the pile meets a refusal at 19m, and the average penetration speed is 82mm/s. For 20% dissipation, the time for 27m penetration is 119.97s, of which the rate is 225mm/s. For the no dissipation case, the time for 27m is 46.45s, and the average speed is 580mm/s. It can be seen from the figure that the addition of the dissipation coefficient greatly slows down the accumulation of excess pore water pressure and thus increases the time required for penetration. And in the future studies, the dissipation analysis is strongly recommended to carry out.
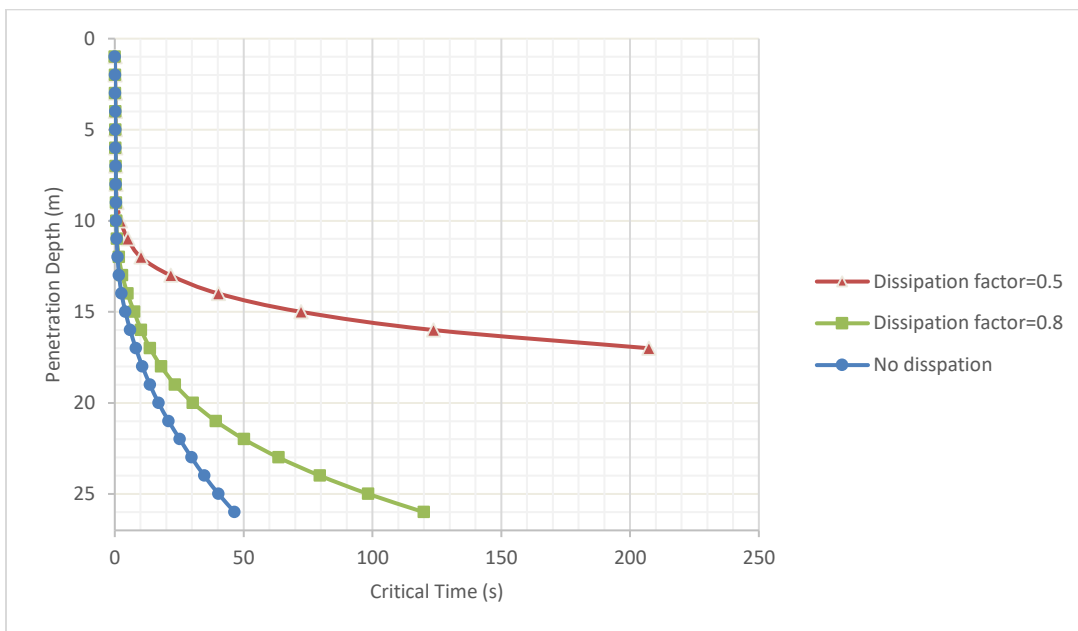
Figure 38 Predicted critical time for different dissipation factors

6.4 Sensitivity Analysis of Internal Shaft Friction

During the vibratory installation, the waves propagating inside the pile also cause pore pressure generation between walls. The pore pressure inside and outside the wall is different. Since the distance between the inner walls of piles is very short, the wave bounces back and forth when it touches the pile wall, so the wave inside the pile shaft is much denser, and the pore pressure generates more rapidly inside the pile. In addition, the pore water inside cannot dissipate easily due to the constraint of the wall. The pore pressure inside may rise more rapidly and have nowhere to dissipate. Thus, it is rational to investigate the prediction result when we assume the inner friction is zero.

The comparison of with and without considering the inner friction is shown in Fig.39, the penetration time of the inner friction case is 331.79s, nearly 3times of the other one, 119.97s. More than double the internal friction resistance increases the penetration time.
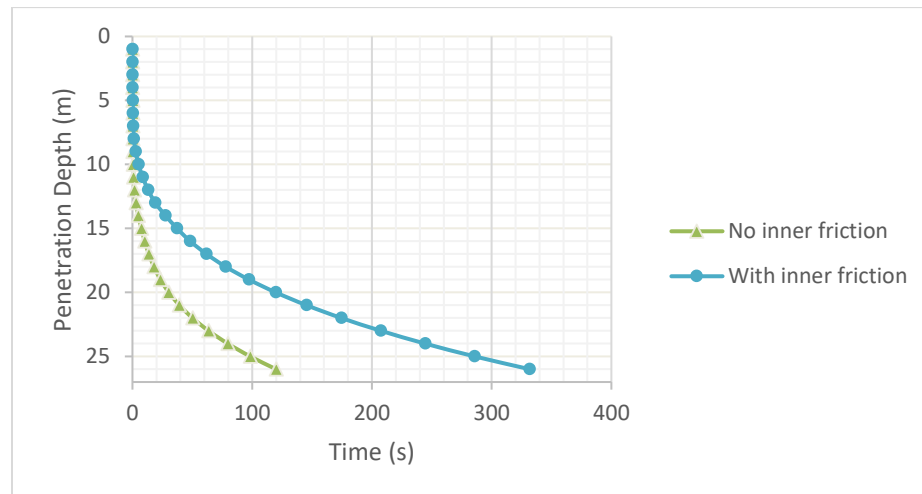
Figure 39 The critical time for cases with/without internal friction

CHAPTER VII

CONCLUSIONS AND FUTURE WORKS

7.1 Conclusions of the study

- The WASD model works well in saturated sands rather than in partial saturated sands and clays. Under the cyclic loading of the vibration force, the pore pressure rises rapidly during the first several seconds and can reduce the effective stress by up to 80%. When the vibration cycles exceed 100 times, the pore pressure accumulation slows down dramatically.

- The penetration time is composed of the critical time for decreasing the soil stiffness and the basic time governed by the equipment and operational procedures (e.g., the rate at which the crane operator feeds the line on which the hammer is suspended). For soft soils, the basic time is the main part of the penetration time, while for the dense soils, the pile needs more time to generate pore pressure and weaken the soil, so the critical time is the governing part.

- The driving ability is positively related to the weight of the hammer: the heavier the hammer is, the stronger the driving ability is, the shorter the penetration time is, and the faster the speed is. There is a negative correlation between pile driving ability and pile weight: the larger the pile size is, the weaker the pile driving ability is, the longer the penetration time is, and the slower the speed is.

7.2 Future Work

To modify the vibratory pile installation model, several research works are required:

- The dissipation analysis for saturated sands during vibratory driving needs to be added.

- The wave propagating inside the pile should be simulated and the inner friction should be computed quantitively.

- The wave propagating axially along the pile should be simulated with considering the compressibility of the pile, and the tip resistance degradation needs to be analyzed.

- A saturation factor could be added to work for the partially saturated sands.

REFERENCES

Axelsson, Gary, (2000), "Long-Term Set-up of driven Piles in Sand", Ph.D. thesis 1035, Div. of Soil and Rock Mechanics, Royal Inst. of Technology, Stockholm, Sweden, 194 pp.

Barkan, D.D., (1957), "Foundation Engineering and drilling by the vibration method", Proc. 4th Int. Conf. on Soil Mechanics and Foundation Engineering, Vol. II, London, pp. 3-7.

Bender, C.H., Lyons, C.G., and Lowery, L.L., (1969), "Applications of Wave-Equation Analysis to Offshore Pile Foundations", Proceedings of the First Offshore Technology Conference, Dallas, TX. OTC 1055.

Bosscher, P.J., et al., (1998), "Estimating Bearing Capacity of Piles Installed with Vibratory Drivers ", USACE, CPAR-GL-98-2.

Briaud, J. L. (2013), "Geotechnical engineering: unsaturated and saturated soils", John Wiley & Sons, New York.

Cao, W. & Chen, Y. & Wolfe, W., (2014), " New Load Transfer Hyperbolic Model for Pile-Soil Interface and Negative Skin Friction on Single Piles Embedded in Soft Soils", International Journal of Geomechanics. 14. 92-100. 10.1061/ (ASCE)GM. 1943-5622.0000289.

Chua, K.M., Gardner, S., and Lowery, L.L., (1987), "Wave Equation Analysis of a Vibratory Hammer-Driven Pile", Presented at the 19th Annual Offshore Technology Conference, Houston, TX. OTC 5396.

Dobry, R., et al. (1982). "Prediction of Pore Water Pressure Buildup and Liquefaction of Sands During Earthquakes by the Cyclic Strain Method." National Bureau of Standards Building Science Series 138, July 1982, 150 pp.

Dorp, R.V, et al., (2019), "Predictions and Monitoring of Installation of Offshore Foundation Monopiles for Windfarms", Presented at the Offshore Technology Conference, Houston, TX. OTC 29400-MS.

Duncan, J.M., Chang, C.Y., (1970), "Nonlinear analysis of stress and strain in soils", Journal of the Soil Mechanics and Foundations Division, ASCE Vol.96 (SM5),1629-1653.

Finn, W.D.L., (1981), "Liquefaction Potential: Developments Since 1976", International Conferences on Recent Advances in Geotechnical Engineering and Soil Dynamics. 17.

Green, R., Cubrinovski, M., Cox, B., & et al. (2014), "Select Liquefaction Case Histories from the 2010–2011 Canterbury Earthquake Sequence", Earthquake Spectra. 30. 131-153. 10.1193/030713EQS066M].

Holeyman, A. (1985) "Dynamic non-linear skin friction of piles", Proceedings of the International Symposium on Penetrability and Drivability of Piles, San Francisco, 10 August 1985, Vol. 1, pp. 173-176.

Holeyman, A., Christian, L., (1997) "Soil-structure interaction during vibratory driving", Proceedings of the Fourteenth International Conference on Soil Mechanics and Foundation Engineering, A.A. Balkema: Rotterdam 1997, p.pp. 817-822.

Hwang, J. H., Chen, C. H., (1995), "A Simple Model for Pore Pressure Build-Up of Soil Under Dynamic Loadings", International Conferences on Recent Advances in Geotechnical Earthquake Engineering and Soil Dynamics. 5.

Ishibashi, I., Sherif, M.A., and Tsuchiya, C., (1977), "PORE-PRESSURE RISE MECHANISM AND SOIL LIQUEFACTION", SOILS AND FOUNDATIONS, Japanese Society of Soil Mechanics and Foundation Engineering, Vol.17, No. 2.

Jonker, G., (1987), "Vibratory Pile Driving Hammers for Pile Installations and Soil Improvement Projects", Presented at the 19th Annual Offshore Technology Conference, Houston, TX. OTC 5422.

Kondner, R.L. (1963) "Hyperbolic stress-strain response: cohesive soils", Journal of the Soil Mechanics and Foundation Division. ASCE, Vol.89, SM.1, pp. 115-143.

Kondner, R.L., Zelasko, J.S., (1963), "A hyperbolic stress-strain formulation for sands", Proceedings of 2nd Pan-American Conference Soil Mechanics and Foundation Engineering, pp. 289-324.

Konstadinou, M., (2013), "Prediction of pore water pressure generation leading to liquefaction under torsional cyclic loading", Soils and Foundations, The Japanese Geotechnical Society, 54(5):993-1005, 2014.

Lade, Poul. (2005), "Overview of Constitutive Models For Soils", Geotechnical Special Publication, pp. 1-34.

Lorenz, H., (1960), Grundbau-Dynamic., Berlin, 308 pp., ISBN 992-449378-8.

Lowery, L.L., Edwards, T.C., and Finley, J.R., (1969), "Increasing the Ability to Drive Long Off-shore Piles", Proceedings of the First Offshore Technology Conference, Dallas, TX. OTC 1064.

Martin, G. R., Finn, W. D. L., and Seed, H. B. (1975), Fundamentals of liquefaction under cyclic loading, Journal of the Geotechnical Engineering Division, ASCE, Vol. 101(5), 423–438.

Massarsch, K.R., Fellenius, B.H., and Bodare, A., (2017), "Fundamentals of the vibratory driving of piles and sheet piles", Geotechnik, Ernst & Sohn Verlag, Berlin, pp. 1-16.

Negro, Vicente, & Lopez-Gutierrez, Jose & et al. (2017). "Monopiles in offshore wind: Preliminary estimate of main dimensions. Ocean Engineering", 133. 253-261. 10.1016/j.oceaneng.2017.02.011.

Novak M., (1974), "Dynamic stiffness and damping of piles", Canadian Geotechnical Journal 11(4): 574-598

Oneill, M.W., Vipulanandan, C., (1989a), "Laboratory evaluation of piles installed with vibratory drivers", National Cooperative Highway Research Program, Report No. 316, National Research Council, Washington, DC. Vol. 1. pp. 1-51. ISBN 0-309-04613-0.

Potts, D.M., Zdravkovic ́, L.T., (1999), "Finite element analysis in geotechnical engineering: theory", Thomas Telford, London.

Rausche, F., (2002), "Modeling of vibratory pile driving", Vibratory Pile Driving and Deep Soil Compaction. Balkema Publishers, Lisse, p. 123-131

Salgado, R., Bisht, V., & Prezzi, M. (2017), "Pile driving analysis for pile design and quality assurance (Joint Transportation Research Program Publication No. FHWA/IN/JTRP-2017/15)", West Lafayette, IN Purdue University. https://doi.org/10.5703/1288284316514

Seed, H. B., P. P. Martin, and L. Lysmer, (1976), "Pore Water Pressure Changes During Soil Liquefaction," ASCE, J.G.E.D., Vol. 102, No. GT4, pp. 323-346.

Shahnazari, H., Dehnavi, Y., Alavi, A., (2010), "Numerical modeling of stress-strain behavior of sand under cyclic loading. Engineering Geology", Vol.116. pp.53-72.

Smith, E.A.L., (1960), "Pile-driving analysis by the wave equation", Journal of the Soil Mechanics and Foundations Divisions, ASCE, Vol. 86, August 1960.

Ti, K.S., et al., (2009), "A review of basic soil constitutive models for geotechnical application", Electronic Journal of Geotechnical Engineering, pp. 14-18.

Truong, P., (2012), "Dynamic soil mass and resonant frequency of pile foundations", 14th Asian Regional Conference on Soil Mechanics and Geotechnical Engineering.

Viking, K., (2002), "Vibro-drivability, a field study of vibratory driven sheet piles in non-cohesive soils", Ph.D. thesis, Div. Of Soil and Rock Mechanics, Royal Inst. of Technology, Stockholm, Sweden.

Vucetic, M., (1994), "Cyclic Threshold Shear Strains in Soils", Journal of Geotechnical Engineering/ Volume 120 Issue 12

Warrington, D. (2006), "Development of a Parameter Selection Method for Vibratory Pile Driver Design with Hammer Suspension." 10.13140/ RG.2.2.20778. 67522.

Warrington, D.C., (1989), "Theory and Development of Vibratory Pile-Driving Equipment", Presented at the 21st Annual Offshore Technology Conference, Houston, TX. OTC 6030.

Zhou. P, (1993), "Numerical Analysis of Electromagnetic fields", Springer-Verlag Berlin Heidelberg, New York.

MATLAB PROFILE: MAIN ROUTINE

```matlab
%program for horizontal propagation of shear waves
%in axisymmetric system
%implicit (Euler backward difference) version
%stress-strain law is nonlinear (hyperbolic)
%along the pile
clear all
%inputs
%loading
moment=320;                          %eccentric moment
kg.m
m_v=54000;                           %mass of vibrator                      kg
m_p=126000;                          %mass of pile                          kg
mass=m_v+m_p;                        %total mass of vibratory part          kg
f=20;                                %load frequency                        Hz
ubamp=moment/mass;                   %vibrating amplitude                   m
%soil properties
density=1837;                        %density
kg/m3
effective_unit_weight=8200;          %effective unit weight for dense sand
N/m3
r0=2;                                %pile radius                           m
thick=0.046;                         %thickness of wall                     m

Atip=pi*r0*r0-pi*(r0-thick)^2;       %tip area
rmax=ubamp*100000;                   %far field (set rmax=20000*ub)         m
rmax=round(rmax);
FR=0.01;                             %average friction ratio along shaft
qc=14000000;                         %initial cone resistance
pa
Gmax_initial=15*qc;                  %initial shear modulus                 pa
vs=sqrt(Gmax_initial/density);       %shear wave velocity                   m/s
%discretization
lambda=vs/f;                         %wavelength                            m
deltar=0.5;                          %calculate per 0.5 meters              m
npt=(rmax-r0)/deltar;                %number of points in spatial domain
dp=15;                               %penetration depth
Atime=zeros(1,dp);                   %time for every penetration
Acctime=zeros(1,dp);                 %accumulation time

for i=2:npt
        r(i)=r0+(i-1)*deltar;        %radial coordinates of FD points
end
r(1)=r0;
T=1/f;                               %period
deltat=T/10;                         %time step (10/period)
nstep=2000;                          %number of time steps
tmax_store=zeros(dp,nstep);
%plotting
plotfreq=10;                         %frequency of plottting wave profiles for every
cycle
%preprocessing
omega=2*pi*f;                        %angular frequency
kstiff(npt,npt)=zeros;               %static stiffness matrix
kstiff_initial(npt,npt)=zeros;       %initial static stiffness matrix
R(npt,1)=zeros;                      %load vector
u(npt,1)=zeros;                      %displacement
dlnGdrc(npt,1)=zeros;                %derivative of G
excess_pwp_store=zeros(npt,nstep);   %store matrix of excess pore water pressure
```

```matlab
effective_stress=zeros(npt,nstep);

%construct unchanging components of stiffness matrix

for depth=1:dp                              %penetration loop


for ii=1:depth                              %vibration loop
    if ii<6
        qc=19000000;                        %input uncorrected cone resistance
pa
    elseif ii>=6&&ii<9
        qc=11000000;
    elseif ii>=9
        qc=18000000;
    end
    if ii==4
        qc=31000000;
    end

sigma0=effective_unit_weight*ii;            %overburdon pressure
pa

Gmax_initial=15*qc;                         %initial shear modulus
pa
fs=FR*qc;                                    %average sleeve friction
pa
tmax_initial=fs*(0.65+0.35*tanh(1.5*(FR-0.02))); %initial ultimate shear stress
pa
for i=2:npt-1
    kstiff_initial(i,i-1)=1/deltar^2-1/(r(i)*2*deltar);    %left of diagonal
    kstiff_initial(i,i)=-2/deltar^2;                        %diagonal
    kstiff_initial(i,i+1)=1/deltar^2+1/(r(i)*2*deltar);    %right of diagonal
end

%time stepping
%prepare for variable G
G=Gmax_initial*ones(npt,1);             %initial distribution of G
G_tangent=G;
dlnGdr=zeros(npt,1);

    for i=1:npt-1
     dlnGdr(i)=(log(G(i+1))- log(G(i)))/deltar;
    end


%initialize
t=0;
displacement_plus_dt=zeros(npt,1);          %displacement at time t+deltat
displacement_t=zeros(npt,1);                %displacement at time t
displacement_minus_dt=zeros(npt,1);         %displacement at time t-deltat
R(npt,1)=zeros;                             %load vector
strain_minus_dt=zeros(npt,1);               %strains at previous time step tm1
strain_t=zeros(npt,1);                      %strains at current time t
strain_rev=zeros(npt,1);                    %most recent strain reversal
backbone=ones(npt,1);                       %1=on backbone curve, 2=unload-reload

for k=1:nstep
    %modify stiffness for variable G
    for i=2:npt-1
        kstiff(i,i-1)=G_tangent(i)*(kstiff_initial(i,i-1)-1/(2*deltar)*dlnGdr(i));   %left
        kstiff(i,i)=G_tangent(i)*kstiff_initial(i,i);                                %diagonal
        kstiff(i,i+1)=G_tangent(i)*(kstiff_initial(i,i+1)+1/(2*deltar)*dlnGdr(i));
%right
    end
    %composite K-matrix
    vs_t=sqrt(G_tangent(i)/density);            %shear wave velocity at time t
    A=deltar/(vs_t*deltat);                     %coefficient for viscous far field
boundary
```

```matlab
    Kcomp=deltat^2/density*kstiff-eye(npt,npt);
    %modify Kcomp for boundary constraints
    Kcomp(1,1)=1;
    Kcomp(npt,npt)=1+A;
    Kcomp(npt,npt-1)=-1;
    t=t+deltat;                     %update time
    tstore(k)=t;
    ub=ubamp*sin(omega*t);          %applied boundary displacement
    R=-2*displacement_t+displacement_minus_dt;          %load vector
    R(1,1)=ub;
    R(npt,1)=A*displacement_t(npt,1);
    displacement_plus_dt=Kcomp\R;
    %update
    displacement_minus_dt=displacement_t;
    displacement_t=displacement_plus_dt;

    %compute strains
    strain_field;
    %-------------------------------------------------------------------------------
-----------------------%
    %-------------------------------------------------------------------------------
-----------------------%
    %-------------------------------------------------------------------------------
-----------------------%
    %pore water pressure based on strain
 N=t*f;
normalized_pwp=zeros(npt,1);            %normalized pore water pressure
pwpstoretop=zeros(npt,1);
pwpstorebot=zeros(npt,1);               %pore water pressure
strain_max=zeros(npt,1);                %shear strain amplitude
lgstrain_max=zeros(1,npt);
%input pore water pressure curve:
    cyclic_amp=[0 0.00001 0.00003 .00005 .0001 0.0003 0.0005 0.001 0.003 0.1];
    pwpn1=[0 0.000 0.000 0.000 0.0015 0.05 0.07 0.1 0.18 0.3];          % curve N=1
    pwpn5=[0 0.000 0.000 0.000  0.002 0.07 0.17 0.3 0.55 0.64];         % curve N=5
    pwpn10=[0 0.000 0.000 0.000  0.002 0.09 0.2 0.38 0.74 0.79];         % curve N=10
    pwpn30=[0 0.000 0.000 0.000  0.002 0.12 0.27 0.51 0.9 0.96];         % curve N=30
    pwpn100=[0 0.000 0.000 0.000 0.002 0.14 0.38 0.84 0.95 0.999];        % curve N=100
    lgcyclic_amp=log10(cyclic_amp);                                       %shear
strain in log scale
    lgcyclic_amp(1)=-10;

 for i=2:npt-1

        strain_max(i)=max(abs(strain_store(i,1:k)));

 strain_maxstore(i,k)= strain_max(i);
     if strain_max(i)>(10^-6)
        lgstrain_max(i)=log10(strain_max(i));
 %select pwp curve
            if N>0&&N<=1
              normalized_pwp(i)=0;
            elseif  N>1&&N<=5
              pwpstoretop(i)=interp1(lgcyclic_amp,pwpn5, lgstrain_max(i));
              pwpstorebot(i)=interp1(lgcyclic_amp,pwpn1, lgstrain_max(i));
              normalized_pwp(i)=pwpstorebot(i)+(pwpstoretop(i)-pwpstorebot(i))/(log10(5)-
log10(1))*(log10(N)-log10(1));
            elseif  N>5&&N<=10
              pwpstoretop(i)=interp1(lgcyclic_amp,pwpn10, lgstrain_max(i));
              pwpstorebot(i)=interp1(lgcyclic_amp,pwpn5, lgstrain_max(i));
              normalized_pwp(i)=pwpstorebot(i)+(pwpstoretop(i)-
pwpstorebot(i))/(log10(10)-log10(5))*(log10(N)-log10(5));
            elseif  N>10&&N<=30
              pwpstoretop(i)=interp1(lgcyclic_amp,pwpn30, lgstrain_max(i));
              pwpstorebot(i)=interp1(lgcyclic_amp,pwpn10, lgstrain_max(i));
              normalized_pwp(i)=pwpstorebot(i)+(pwpstoretop(i)-
pwpstorebot(i))/(log10(30)-log10(10))*(log10(N)-log10(10));
            elseif  N>30&&N<=100
              pwpstoretop(i)=interp1(lgcyclic_amp,pwpn100, lgstrain_max(i));
```

```
                pwpstorebot(i)=interp1(lgcyclic_amp,pwpn30, lgstrain_max(i));
                normalized_pwp(i)=pwpstorebot(i)+(pwpstoretop(i)-pwpstorebot(i))/(2-
log10(30))*(log10(N)-log10(30));
            elseif N>100
                pwpstorebot(i)=interp1(lgcyclic_amp,pwpn100, lgstrain_max(i));
                normalized_pwp(i)=pwpstorebot(i)+(log10(N)-log10(100))*0.35;
            end
        elseif strain_max(i)<=(10^-6)
            normalized_pwp(i)=0;
        end
        excess_pwp_store(i,k)=normalized_pwp(i)*sigma0;            %excess pore water
pressure
end
                if ii==5
                    normalized_pwp(i)=0;
                end
        tip_r(1,k)=0.25*qc*(1-normalized_pwp(2))*Atip;            %tip resistance   kN
%-------------------------------------------------------------------------------
--------------------%
%-------------------------------------------------------------------------------
--------------------%

F_dr(k)=mass*9.8+moment*omega*omega*sin(t);                        %driving force   kN

    %update G
    Gtangent;
    tmax_store(ii,k)= tmax(2,k);                                   %record the t_max
along the pile for k timestep

    for i=2:npt-1
        dlnGdr(i)=(log(G_tangent(i+1))- log(G_tangent(i-1)))/(2*deltar);
    end

end
end


total_fric=zeros(1,nstep);                                        %total friction along
the pile

F_re=zeros(1,nstep);                                              %total resistance force


for jj=2:k

    total_fric(jj)=sum(tmax_store(:,jj))*2*pi*(r0+r0-thick);
    F_re(jj)=total_fric(jj)+tip_r(jj);
    DT2(jj)=F_re(jj)-F_dr(jj);
    if DT2(jj)<10^-5
        break
    end
end


Atime(depth)=(jj-1)*deltat;
if Atime(depth)<T
    Atime(depth)=T;
end
Acctime(depth)=sum(Atime(1:depth));

end
```

APPENDIX B

SUBROUTINE: STRAIN FIELD

```
%subroutine to compute strain distribution
%checks for strain reversals
%stores current strains in vector gammat
%stores previous strains in vector gammatm1
strain_minus_dt=strain_t;
for i=2:npt-1
    strain_t(i)=(displacement_t(i+1)-displacement_t(i-1))/(2*deltar);
    if abs(strain_t(i)) <= abs(strain_minus_dt(i))
        %record strain reversal
        strain_rev(i)=(strain_t(i)+strain_minus_dt(i))/2;
        %record that no longer on backbone curve
        if backbone(i)==1
            backbone(i)=2;
        end
    end
    %store strain history
    strain_store(i,k)=strain_t(i);
end
```

APPENDIX C

SUBROUTINE: TANGENT SHEAR MODULUS

```matlab
%subroutine to compute tangent shear stiffness
%hyperbolic stress-strain law

delta_strain=abs(strain_t-strain_rev);
Gmax=zeros(npt,1);
sigma_initial=effective_unit_weight*depth*ones(npt,1);
tmax=zeros(npt,1);
for i=2:npt-1
   effective_stress(i,k)=sigma_initial(i)-excess_pwp_store(i,k);      % stress reduced by
excess pwp
    effective_str_store(i,k)= effective_stress(i,k);
   Gmax(i)=Gmax_initial*abs(effective_stress(i,k)/sigma_initial(i))^0.5;
   tmax(i)=tmax_initial*abs(effective_stress(i,k)/sigma_initial(i));
    if backbone(i)==1            %backbone 1st loading
        xi(i)=delta_strain(i)/tmax(i);
    elseif backbone==2
        xi(i)=delta_strain(i)/(2*tmax(i));     %subsequent unload-reload
    end
    eta(i)=1/Gmax(i)+xi(i);
    G_tangent(i)=1/eta(i)-xi(i)/eta(i)^2;
end
```